On the mechanisms of jet-installation noise reduction with flow-permeable trailing edges

Rego, Leandro; Avallone, Francesco; Ragni, Daniele; Casalino, Damiano

DOI
10.1016/j.jsv.2021.116582

Publication date
2022

Document Version
Final published version

Published in
Journal of Sound and Vibration

Citation (APA)
Rego, L., Avallone, F., Ragni, D., & Casalino, D. (2022). On the mechanisms of jet-installation noise reduction with flow-permeable trailing edges. *Journal of Sound and Vibration*, *520*, Article 116582. https://doi.org/10.1016/j.jsv.2021.116582

Journal of Sound and Vibration 520 (2022) 116582

Contents lists available at ScienceDirect

Journal of Sound and Vibration

journal homepage: www.elsevier.com/locate/jsvi

On the mechanisms of jet-installation noise reduction with flow-permeable trailing edges

Leandro Rego [*], Francesco Avallone, Daniele Ragni, Damiano Casalino

Delft University of Technology, Department of Aerodynamics, Wind Energy and Propulsion, Kluyverweg 1, 2629 HS, Delft, The Netherlands

ARTICLE INFO

Keywords:
Aeroacoustics
Jet-installation noise
Porous materials

ABSTRACT

This paper investigates the mechanisms by which flow-permeable materials provide noise reduction in an installed jet configuration. Numerical simulations are carried out with a flat plate placed in the near field of a single-stream subsonic jet ($M_a = 0.3$ and $M_a = 0.5$). The trailing-edge region of the plate is replaced by three different permeable structures, with different properties: a metal foam, a perforated plate and a diamond-shaped structure. Due to its complex geometry, the metal foam is modeled with an equivalent region governed by Darcy's law. The perforated plate has the highest resistivity among all investigated configurations, whereas the metal foam and diamond inserts have similar properties. Far-field spectra show significant noise reduction when the solid trailing edge is replaced with the permeable materials, with a maximum decrease of 12 dB at $St = 0.12$, for $M_a = 0.5$. Beamforming results show that the dominant acoustic source is located at the solid–permeable junction for the metal foam and diamond structures, whereas the perforated one has the source positioned near the trailing edge, similarly to the solid case. A breakdown of the far-field noise generated by the plate is also performed, where the contributions from the solid and permeable sections are computed separately. The former has distinct regions in the noise spectrum, which are dominated either by surface pressure fluctuations or trailing-edge scattering. However, for the permeable region, the results point to a significant mitigation of the noise due to scattering, which is no longer the dominant mechanism in any frequency range. This is confirmed by lower values of spanwise coherence, computed from the surface pressure, for the permeable trailing edge, compared to the solid case. Therefore, the clear dominant mechanism in the permeable region of the plate is the unsteady loading to pressure wave impingement. This is verified for all investigated configurations so that even with a low permeability structure, significant noise reduction can still be achieved.

1. Introduction

Aircraft noise levels have been significantly reduced with the introduction of high-bypass ratio turbofan engines, particularly the noise generated by turbulent mixing between the exhaust flow and ambient air [1]. Turbulence-mixing noise has a strong dependence on the jet flow speed ($\propto U_j^8$) [2], and thus, it can be substantially mitigated by increasing the bypass ratio. This, however, leads to larger engines and an increased proximity to the airframe lifting surfaces. The interaction between the engine exhaust flow and a nearby surface generates an acoustic source known as Jet-Installation Noise (JIN) [3,4]. This source is generated by convecting hydrodynamic pressure waves in the mixing layer impinging on the surface; the resultant unsteady surface pressure translates into

---

[*] Corresponding author.
E-mail address: l.rego@tudelft.nl (L. Rego).

https://doi.org/10.1016/j.jsv.2021.116582
Received 9 March 2021; Received in revised form 7 July 2021; Accepted 22 October 2021

noise in the far field, equivalent to a distribution of acoustic dipoles with intensity proportional to U_j^6 [5]. Moreover, due to the geometric discontinuity at the surface trailing edge, those hydrodynamic fluctuations are also scattered as noise to the far field with a cardioid directivity pattern and intensity proportional to U_j^5 [6,7]. This phenomenon is responsible for noise increase at low and mid frequencies, particularly in the directions normal and upstream of the jet axis [8,9]. Installation effects also account for reflection of acoustic waves from the jet itself on the surface [10] and acoustic shielding on the opposite side of the surface [11]. Computational results of aircraft acoustic footprint have shown that installation effects are responsible for penalties of approximately 4 EPNdB at full aircraft level [12]. Therefore, the development of noise reduction solutions for this particular source is of interest, as well as understanding the phenomena behind the sound mitigation.

A solution for JIN reduction is the application of flow-permeable materials on the scattering surface. Rego et al. [13] show through acoustic measurements that noise reductions on the order of 9 dB are achieved by replacing the solid trailing edge of the surface with a permeable structure. In the experiments, two permeable configurations are investigated: a metal foam and a perforated plate. In terms of noise mitigation, the former performs better, particularly in the frequency range where JIN is the dominant source, likely due to a better pressure balance between the upper and lower sides of the plate [13]. It is believed that the junction between solid and porous regions of the plate becomes a new scattering location and the dominant source for certain frequencies [13], but this hypothesis has not been confirmed yet. Moreover, those results could not determine with certainty how the noise due to surface pressure fluctuations and trailing-edge scattering are affected separately by the flow-permeable materials, as well as which properties of the permeable materials are the most relevant for noise reduction.

One of the properties by which permeable materials provide noise reduction is the flow communication between the two sides of the surface. This condition has been shown to be important for flap side-edge [14] and turbulent boundary-layer trailing-edge (TBL-TE) noise reduction [15], as it allows an improvement of the pressure balance around the surface. The flow communication and consequent pressure balance are dependent on parameters such as porosity and resistivity. Through airfoil TBL-TE noise measurements, Sarradj and Geyer [16] have shown that these parameters affect the frequency range and amplitude of noise reduction, as well as the aerodynamic characteristics of the airfoil, resulting in lift reduction and drag increase. An analytical study by Jaworski and Peake [17] on the scattering mechanism of a surface with a permeable trailing edge has shown that the dependence of the noise levels with flow velocity changes from U^5 for the solid case to U^6 for the permeable one. This result indicates that the scattering mechanism becomes weaker with a permeable surface. In terms of material micro-structure, Rubio-Carpio et al. [18] has studied TBL-TE noise reduction by replacing a section of the trailing edge (last 20% of the chord) with porous inserts manufactured out of metallic foams. Acoustic beamforming results show noise reduction at low and mid frequencies, on the order of 10 dB with respect to the solid airfoil [18]. Moreover the dominant source location has shifted from the original trailing-edge position to the solid–permeable junction, which becomes the dominant acoustic scattering region [18]. Although well characterized for those applications, it is not yet clear how the properties of the permeable materials affect the near-field unsteady flow around the plate in an installed jet configuration, and the associated JIN generation mechanisms, i.e. noise due to pressure wave impingement and trailing-edge scattering.

Therefore, this work investigates the flow field and acoustic characteristics of an installed jet configuration of a surface with a permeable trailing edge. The pressure field on the plate and the unsteady flow rate through the permeable material allow for an assessment of its properties, such as resistivity, on the final noise signature. These results, combined with an analysis of acoustic directivity and source localization through beamforming, also provide information on how each of the noise mechanisms are affected by the permeable structures, as well as the effect of the solid–porous junction in the plate. This study is carried out via numerical simulations, using a lattice-Boltzmann solver coupled with a Very Large Eddy Simulation model (LBM-VLES). This method has been chosen since it can resolve the flow field with a relatively low computational cost, still showing very good agreement with experimental data [9]. The installed jet configuration investigated in this paper replicates the one from Rego et al. [13], and the experimental results from that reference are used for validation of the installed jet set-up with flow-permeable trailing edges.

This paper is organized as follows. In Section 2, the flow simulation model is discussed, with a brief description of the LBM-VLES. In Section 3, the studied cases and the computational set-up are described, along with the characteristics of the investigated flow-permeable structures. In Section 4, the results are discussed, focusing on the physical effects of flow-permeable trailing edges on JIN reduction, based on far- and near-field results. Finally, the most important findings of this work are summarized in the conclusions.

2. Flow solver

The Lattice-Boltzmann Method (LBM) solves the discrete form of the Boltzmann equation by using particle distribution functions to simulate the macroscopic flow properties. Through local integration of these particle distribution functions, the flow density, momentum and internal energy are obtained [19]. The solution of the Boltzmann equation is performed on a Cartesian mesh (lattice), with an explicit time integration and collision model:

$$f_i(\boldsymbol{x} + \boldsymbol{c}_i \Delta t, t + \Delta t) - f_i(\boldsymbol{x}, t) = C_i(\boldsymbol{x}, t), \tag{1}$$

with f_i representing the particle distribution function along the ith lattice direction. The particle motion is statistically described at a position $\boldsymbol{x}$ with a discrete velocity $\boldsymbol{c}_i$, in the i-direction at the time t. The space and time increments are represented by $\boldsymbol{c}_i \Delta t$ and Δt, respectively. For the collision term $C_i(x, t)$, the employed formulation is based on a Galilean invariant for thermal flows of non-unitary Prandtl number [20]. The adopted equilibrium distribution function f_i^{eq} consists in small velocity expansions of the Maxwell–Boltzmann distribution [21]. The distribution functions are projected on a basis of Hermite orthogonal polynomials in velocity space. This is performed because the expansion coefficients are exactly the velocity moments of the distribution function, including the macroscopic flow variables such as density and velocity [22]. Due to orthogonality, the series can be truncated at an order 3, in order for the pressure tensor and the momentum dynamics to be accurate at the Navier–Stokes level (second order moments), or 4th order to include modeling of internal energy and heat flux, without altering the low order coefficients and flow quantities. The moments are computed over a discrete set of particle velocities, using Gaussian quadrature formulas for different lattices [20]. For this work, a 19-state lattice (subdivided into 19 nodes), known as D3Q19, is adopted.

Given the high Reynolds number of the jet flow, a Very Large Eddy Simulation (VLES) model accounts for the unresolved scales of turbulence. In a Navier–Stokes formulation, for example in a Large Eddy Simulation (LES), the large scales of turbulence are described with the inclusion of an eddy viscosity term, whereas for LBM a turbulent relaxation time is defined with a term depending on the turbulent kinetic energy, dissipation rate and the local velocity gradient. A modified two-equations $k-\epsilon$ Renormalization Group (RNG) turbulence model is employed to compute this turbulent relaxation time, which is added to the viscous relaxation time [23]:

$$\tau_{\mathrm{eff}} = \tau + C_{\mu}\frac{k^2/\epsilon}{(1+\eta^2)^{1/2}}, \tag{2}$$

where $C_{\mu} = 0.09$, and η is a combination of the local strain, local vorticity and local helicity parameters [24]. The term η allows for the mitigation of the sub-grid scale viscosity, so that the resolved large-scale structures are not numerically damped. This model is not equivalent to solving the $k-\epsilon$ RANS equations, so there is not an explicit modification of the eddy viscosity, but rather a modification of the relaxation process leading to a different eddy viscosity [25]. Hence, the Reynolds stresses are not solved simultaneously with the flow governing equations, but they are a consequence of the particle movement and collision, and thus part of the solution. The Reynolds stresses have then a non-linear structure and are better suited to represent turbulence in a state far from equilibrium, as in the presence of distortion, shear, and rotation [25] and, similarly as the macroscopic flow properties, they can be recovered through the computation of the moment around the particle distribution function. The no-slip wall boundary conditions are modeled with a "bounce-back" mapping of the particle velocities, for which both normal and tangential components are inverted after collision with the surface [26]. A wall function, based on an extension of the generalized law-of-the-wall model, taking into account the effect of pressure gradients [27], is used to model a boundary layer on a solid surface. A more detailed description of the applied formulation can be found in Ref. [28].

The main advantage of using a LBM solver in this study, with respect to a Navier–Stokes formulation, is its inherent low dissipative and dispersive characteristic, which is necessary for the accurate prediction of acoustic perturbations that are usually orders of magnitude lower than the characteristic pressure of a flow [29,30]. An accurate prediction of acoustic wave propagation from source to the far field usually requires high order numerical schemes, however this can be achieved effectively with LBM, which is a second order scheme and less dissipative [30]. Moreover, the adopted process wherein the particle collision occurs locally allows for an easy parallelization of the computation, thus reducing the computational time and cost [29].

The far-field noise is estimated through the Ffowcs-Williams and Hawkings (FWH) analogy [31], adopting the formulation 1 A from Farassat extended to a convective wave equation [32,33]. This approach is implemented in the time domain using a source-time dominant algorithm [34]. In addition, a frequency-domain formulation of the FWH analogy is also performed. This method is based on the one proposed by Lockard [35], extended to a three-dimensional flow field. It is theoretically consistent with the time-domain approach, but Fourier transforms are realized on the FWH source terms before propagation to the far-field [36]. This frequency-domain approach is applied for the computation of a cross-spectral matrix of microphones mounted in a phased array. This matrix is subsequently used in beamforming calculations for acoustic source localization.

A permeable surface is defined to include all the relevant noise sources in the jet and on the plate [9]. Pressure and velocity fluctuations recorded on this surface are used for far-field noise estimation. A more detailed description of the FWH surface is reported in Section 3. In addition, the FWH analogy is applied using the surface pressure fluctuations on the flat plate as input. The resulting sound field is, therefore, only related to the noise mechanisms on the plate (dipole sources) since it does not include the fluctuations generated by the quadrupole sources in the jet.

The methodology described above is implemented in the commercial software Simulia PowerFLOW 6-2019. This software has been also used and validated for aero-engine aeroacoustic applications to predict fan broadband noise in subsonic [37,38] and transonic conditions [39]. A validation study for the isolated SMC000 jet has been accomplished by van der Velden et al. [36], showing a very good agreement with experimental results. For an installed jet, computations have been performed by Rego et al. [9]. The results, in terms of far-field noise spectra, also have shown a good agreement with experimental data, indicating the capability of the solver to accurately predict JIN.

3. Computational set-up

3.1. Installed jet configuration and flow conditions

The baseline configuration studied in this work replicates the installed jet model from the work of Rego et al. [13], where a solid flat plate is placed in the vicinity of a single-stream jet nozzle (SMC000). The SMC000 is a round, convergent nozzle with an exit diameter $D_j = 50.8$ mm, used for studies on subsonic jets [4]. The primary convergent nozzle has a 152 mm diameter inlet, followed by a contraction with a 5° taper angle up to the exit plane. The main geometric configuration investigated in the experiments of Rego et al. [13] is chosen for the simulations of both solid and permeable trailing edges, as shown in Fig. 1. The plate length, which corresponds to the distance between the nozzle exit plane and the trailing edge, is defined as $L = 6D_j$. This value has been chosen in

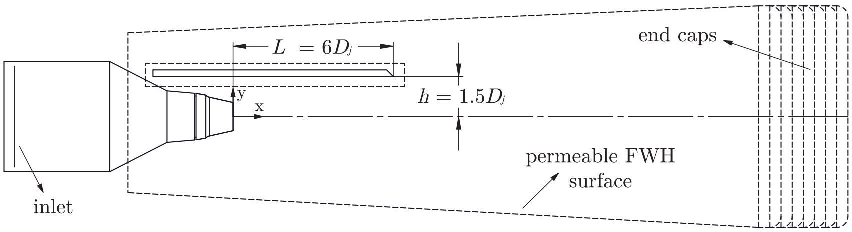

Fig. 1. Installed jet configuration with a flat plate length $L = 6D_j$ and radial position $h = 1.5D_j$. A permeable FWH surface encompasses the jet and the flat plate. Caps are placed at the downstream end of the surface, and cut-outs are placed in the regions of the plate and nozzle.

Table 1
Jet flow conditions in terms of acoustic Mach number (M_a), nozzle pressure ratio (NPR), temperature ratio (T_R) and Reynolds number (Re).

Condition	M_a [-]	NPR [-]	T_R [-]	Re [10^5]
1	0.3	1.067	0.98	3.58
2	0.5	1.196	0.95	5.96

order to emphasize the contribution of JIN to the overall noise generation and ensure that the plate would be the dominant source. Moreover, this geometry allows for a longer permeable section of the plate and consequently a more meaningful study on the flow and noise mechanisms in that region can be carried out. The radial position of the surface with respect to the jet centerline is set as $h = 1.5D_j$. Previous work [9] has also shown that there is no grazing flow on the surface for this configuration. The plate has a thickness $t = 10$ mm and it has a chamfer angle of 40° at the trailing edge. It also extends $3D_j$ upstream of the nozzle exit plane to avoid scattering effects at the leading edge and properly account for noise shielding at shallow upstream angles. In the spanwise direction, the plate has a width of $36D_j$ to avoid side-edge scattering.

Two flow conditions, characterized by subsonic jets with acoustic Mach number ($M_a = U_j/c_\infty$) $M_a = 0.3$ and $M_a = 0.5$, are simulated. The jet flow characteristics are included in Table 1, such as the Nozzle Pressure Ratio (NPR), the temperature ratio T_R (ratio between the jet and ambient static temperatures), and the Reynolds number Re, based on the nozzle exit diameter. Static flow parameters $p_{\mathrm{amb}} = 101325$ Pa and $T_{\mathrm{amb}} = 288.15$ K are chosen for the computations. Due to similarities between trends for the two jet conditions, the results for the remainder of this work are plotted for the $M_a = 0.5$ jet, unless otherwise stated.

3.2. Flow-permeable materials

Different flow-permeable materials are investigated in this work, with distinct micro-structures and properties, in order to assess the effects of geometry and porosity/resistivity in the noise production. The first permeable trailing edge is represented by a porous media model, which simulates the characteristics of an open-cell metal foam. This foam is characterized by a homogeneous NiCrAl micro-structure with a three-dimensional dodecahedron-shaped cell [40]. This strategy is used due to the high geometrical complexity of the micro-structure, and it has been also adopted by Teruna et al. [41] for airfoil TBL-TE noise studies. This porous media model consists of equivalent fluid regions governed by Darcy's law, which states that the flow pressure gradient ∇p through a permeable material is proportional to the local flow velocity $\boldsymbol{u}_f$, as given by Eq. (3) [42]:

$$\nabla p = -\rho \boldsymbol{R} \cdot \boldsymbol{u}_f, \tag{3}$$

where ρ is the fluid density, $\boldsymbol{R}$ is the overall material resistivity, which is comprised of the inertial ($\boldsymbol{R}_I$) and viscous ($\boldsymbol{R}_V$) resistivity components [43], given by:

$$\boldsymbol{R} = \boldsymbol{R}_V + \boldsymbol{R}_I \boldsymbol{u}_f, \tag{4}$$

$$\boldsymbol{R}_V = \frac{\mu}{\rho \boldsymbol{K}}, \qquad \boldsymbol{R}_I = \boldsymbol{C}, \tag{5}$$

where μ is the fluid dynamic viscosity, $\boldsymbol{K}$ is the permeability and $\boldsymbol{C}$ is the form coefficient of the permeable structure. The interface between this equivalent fluid region and the rest of the domain consists in double-sided surfaces similar to a sliding mesh [44]. Moreover, the mass flux at the interface is conserved by making use of the material porosity σ. The porosity is defined as the ratio between the volumetric densities of the flow-permeable material ρ_p and the original solid structure ρ_s, as shown in Eq. (6):

$$\sigma = 1 - \frac{\rho_p}{\rho_s}. \tag{6}$$

To implement the model in the computational set-up, the same strategy adopted by Teruna et al. [41] is applied. The trailing edge is divided into two regions: the PM (porous medium) and the APM (acoustic porous medium). Both regions are governed by Darcy's law, but the latter also takes into account the acoustic absorption of the material [41]. The trailing edge is then replaced by

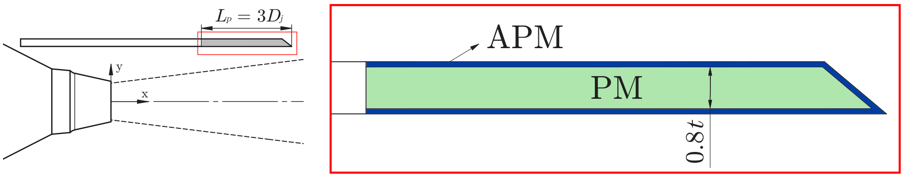

Fig. 2. Flow-permeable trailing edge with length $L_p = 3D_j$. The metal foam trailing edge is modeled with an equivalent Darcy fluid region, comprised by a Porous Medium (PM — inner layer) and an Acoustic Porous Medium (APM — outer layer), which considers the material porosity.

Table 2
Porosity (σ), inertial ($\boldsymbol{R_I}$) and viscous ($\boldsymbol{R_V}$) resistivity parameters applied to the equivalent fluid regions, which replicate the properties of a metal foam with cell diameter $d_c = 800\,\mu\text{m}$.

Region	σ [%]	R_I [m^{-1}]	R_V [s^{-1}]
APM	91.7	2854	6575
PM	–	2520	5489

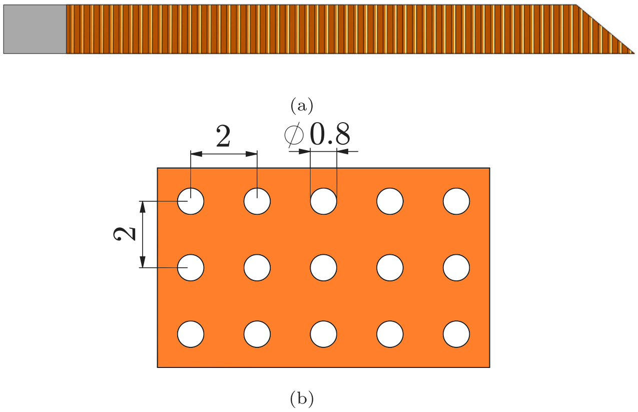

(a)

(b)

Fig. 3. (a) Perforated trailing edge with cylindrical holes. (b) Hole dimensions of the perforated structure. Dimensions in mm.

a PM–APM combination, as shown in Fig. 2. The APM, which includes porosity effects, is placed as an outer layer with thickness $t_{\mathrm{APM}} = 1$ mm on both upper and lower sides, whereas the inner layer is set with PM conditions ($t_{\mathrm{PM}} = 8$ mm). For both regions, the inertial and viscous resistivities are set based on the respective thickness [41], as reported in Table 2. These properties replicate a metal foam structure with cell diameter $d_c = 800\,\mu\text{m}$, equivalent to that investigated by Rego et al. [13]. The resistivities are set the same in all three directions due to the isotropic characteristics of the metal foam.

The second type of flow-permeable structure investigated is a perforated trailing edge, with cylindrical holes normal to the jet axis, connecting the upper and lower sides of the plate, as shown in Fig. 3(a). A configuration with hole diameter $d_h = 800\,\mu\text{m}$ is assessed, as shown in Fig. 3(b), which has been also investigated for JIN reduction by Rego et al. [13].

Finally, a trailing edge with a diamond-shaped micro-structure, based on a tessellation of the cubic cell shown in Fig. 4(a), is also investigated. This cubic cell is built from cylinders with diameter $d_d = 1$ mm, merged at a 120° angle. The purpose of this geometry is to replicate the benefits provided by a metal foam trailing edge, but with a simpler and modular micro-structure, with a clearly defined and repeatable geometry. The final trailing-edge geometry is shown in Fig. 4(b). This configuration also allows for permeability in the axial direction of the jet, as opposed to the perforated trailing edge, for which there is flow only in the radial direction. For the perforated and diamond cases, the actual trailing-edge geometry is simulated, and no porous media model is applied.

The properties of the flow-permeable materials are reported in Table 3, in terms of porosity σ, inertial and viscous resistivity coefficients ($\boldsymbol{R_I}$ and $\boldsymbol{R_V}$, respectively), and the permeability $\boldsymbol{K}$. The original metal foam parameters [18] are included for comparison.

For all configurations, the flow-permeable region of the plate has a length $L_p = 3D_j$ and span $b_p = 6D_j$, centered at the jet symmetry plane, represented by the blue region in Fig. 5. In the measurements performed by Rego et al. [13], the span of the flow-permeable materials was originally $10D_j$. However, it has been verified that shortening this region to $6D_j$ does not change the far-field noise, but highly reduces the computational cost. The area shown in green represents the solid region of the plate where data are sampled (sampling on both upper and lower sides of the surface).

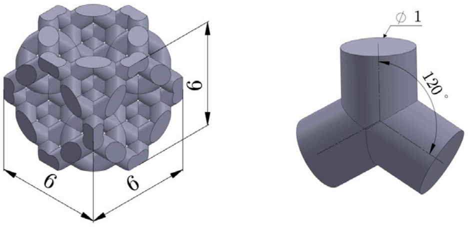

(a)

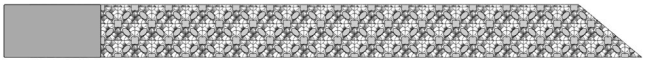

(b)

Fig. 4. (a) Diamond-shaped cubic structure created by the intersection of cylinders with a 1 mm diameter at an angle of 120°. (b) Flow-permeable trailing edge with the diamond structure. Dimensions in mm.

Table 3
Properties of the flow-permeable materials in terms of porosity (σ), inertial ($\boldsymbol{R_I}$) and viscous ($\boldsymbol{R_V}$) resistivity, and permeability ($\boldsymbol{K}$).

Material	σ [%]	R_I [m^{-1}]	R_V [s^{-1}]	K [$\times 10^{-9}$ m^2]
Metal foam	91.7	2612	5390	2.71
Perforated	12.6	7283	9245	1.58
Diamond	61.6	4060	802	18.2

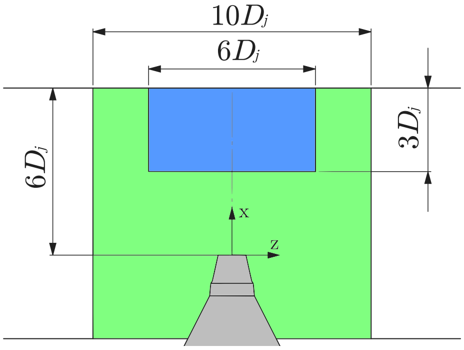

Fig. 5. Dimensions of the flat plate with flow-permeable trailing edge (blue region). The area shown in green represents the solid region of the plate where data is sampled. (For interpretation of the references to color in this figure legend, the reader is referred to the web version of this article.)

3.3. Set-up components and simulation parameters

The computational set-up consists in a nozzle and flat plate placed in an almost quiescent domain (free-stream speed equal to 1% of the jet exit velocity) [9]. To generate the jet flow, an inlet boundary condition is placed $8D_j$ upstream of the nozzle exit plane (Fig. 1). The physical parameters used as boundary conditions are taken from experimental data (Table 1). A zig-zag trip, with a thickness of 1 mm ($0.02D_j$) and spacing of 1.62 mm ($0.03D_j$), is added inside the nozzle, $1.5D_j$ upstream of the exit plane, to force a fully turbulent boundary layer. This set-up has been previously validated for isolated [36] and installed [9] jet analyzes.

The main components of the setup are shown in Fig. 1. A permeable Ffowcs Williams–Hawkings (FWH) surface, represented by dashed lines, is used for the far-field noise computations. This surface extends $22D_j$ downstream of the nozzle exit plane and it has a width of $10D_j$. Cutouts are placed at the nozzle and flat plate regions to avoid spurious effects due to hydrodynamic pressure fluctuations occurring on the FWH. Additional sources caused by the jet crossing the downstream end of the FWH are also mitigated by placing 7 outflow surfaces (or end-caps) (Fig. 1). The far-field pressure signals obtained from each cap (located at different streamwise positions) are averaged, so that the spurious noise produced by the eddies crossing the permeable surface can be removed from the final far-field spectra [45]. Acoustic signals are also obtained from the solid FWH formulation applied to pressure fluctuations on the plate. The sampled region consists in a span of $10D_j$ (similarly as the permeable FWH width), centered at the jet symmetry plane, and the whole plate chord. For the cases with permeable trailing edges, the far-field contributions of the solid and porous sections of the plate can be evaluated separately.

Acoustic sponges (regions of increased viscosity) are added to the set-up in order to prevent wave reflection inside the nozzle and at the boundaries of the computational domain [46]. Inside the nozzle, the sponge extends from the inlet plane up to $3.8D_j$

Table 4
Simulation physical time and acquisition parameters.

Condition	M_a [–]	Physical simulation time [s]	FWH acquisition time [s]	Frequency resolution [Hz]
1	0.3	0.440	0.373	27
2	0.5	0.264	0.224	44

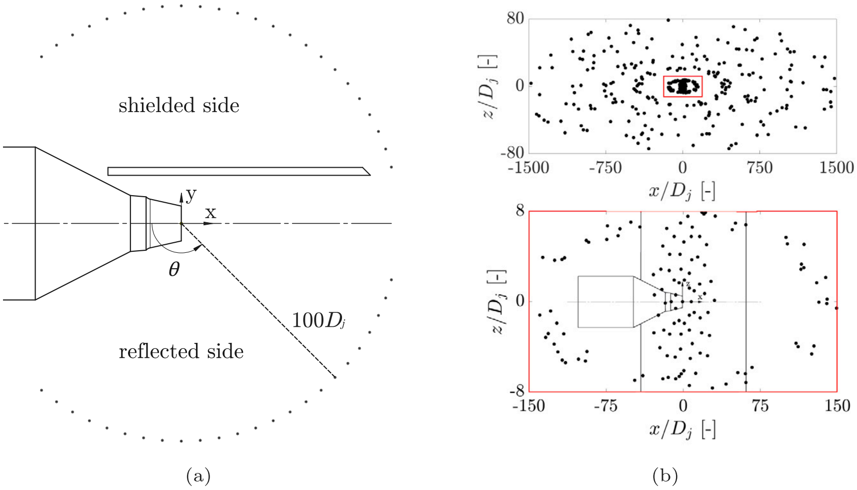

Fig. 6. Far-field microphone positions. (a) 48 microphones in the polar array, divided for the reflected and shielded sides. Microphone distance not to scale (b) 364 microphones in the phased array, parallel to the surface plane. The bottom figure is a zoomed region at the center of the array. Nozzle and plate dimensions not to scale.

upstream of the exit plane. A spherical sponge with a diameter $130D_j$, centered at the nozzle exit plane and encompassing the entire geometry, is also added. A progressive coarsening of the grid towards the boundaries also contributes to the dampening of acoustic wave reflection.

The physical time of the simulations is divided into an initial transient, consisting of 5 flow passes through the FWH surface, and an acquisition time of 27 flow passes (total simulation time of 32 flow passes). The latter is defined based on the minimum output frequency to be analyzed (defined as $St = 0.02$), and the number of spectral averages (defined as 20), for an overlap coefficient of 0.5 in the Fast Fourier Transform (FFT) computation. For the finest grid resolution investigated, the physical time step is 1.5×10^{-7} s. The unsteady pressure on the FWH surface is sampled with a frequency of 72 kHz and 120 kHz for conditions 1 and 2, respectively. The resultant physical simulation time and acquisition parameters are shown in Table 4 for the simulated jet flow conditions. The frequency resolution refers to the minimum frequency band obtained from the FFT of the acoustic signals, based on the acquisition time and the selected number of averages.

The far-field noise levels are computed with a microphone arc array, centered at the nozzle exit plane, with a radius of $100D_j$. Microphones are placed at an interval of 5°, ranging from $\theta = 50°$ to $\theta = 165°$ ($\theta = 180°$ corresponds to the jet axis). The noise levels are evaluated at both shielded and reflected sides of the plate, as shown in Fig. 6(a). Acoustic signals from the solid FWH formulation [31] can be obtained at shallower angles in both downstream and upstream directions, since they are not affected by the end caps and the nozzle, as in the case of the permeable FWH surface.

Acoustic data are also obtained at a microphone phased array for source localization with the beamforming technique [47]. A frequency-domain form of the FWH analogy [35] is applied on the permeable surface data, which provides the cross-spectral matrix for the entire array. The array is located on a plane parallel to the plate surface, at a distance of $20D_j$ from the jet axis on the reflected side, and centered at the nozzle exit plane. The array has 364 microphones arranged in a modified Underbrink multi-arm spiral design [48], with an effective diameter of $3000D_j$ in the streamwise direction and $160D_j$ in the spanwise direction, as shown in Fig. 6(b). The array aperture and location are chosen in order to provide a streamwise spatial resolution of $0.2D_j$ ($0.065L_p$) at a frequency of 300 Hz, based on the Rayleigh criterion equation [49]. The used steering vector formulation is taken from the work of Sijtsma [50] for conventional beamforming, assuming monopole sources. The scan plane is chosen as a square with a $10D_j$ edge on the bottom surface of the plate, and centered at ($5D_j$, $1.5D_j$,0). A grid size of $0.02D_j$ is used in the x- and z-directions.

3.4. Grid convergence and set-up validation

A grid convergence study is performed to assess the sensitivity of the numerical results to the discretization of the computational domain. The mesh resolution is defined as the number of voxels (volumetric cell element or lattice in the domain) at the nozzle exit diameter, and the resultant element size is used throughout the jet plume. Three grids are investigated: coarse (resolution = 32

Table 5
Grid characteristics for convergence analysis for the installed jet configuration with the PM–APM trailing edge.

Grid	Resolution	Voxel size at nozzle exit [mm]	Finest voxel size [mm]	Number of voxels [10^6]	kCPUh
Coarse	32	1.59	0.199	331	18.8
Medium	45	1.13	0.141	647	46.4
Fine	64	0.79	0.099	1688	147

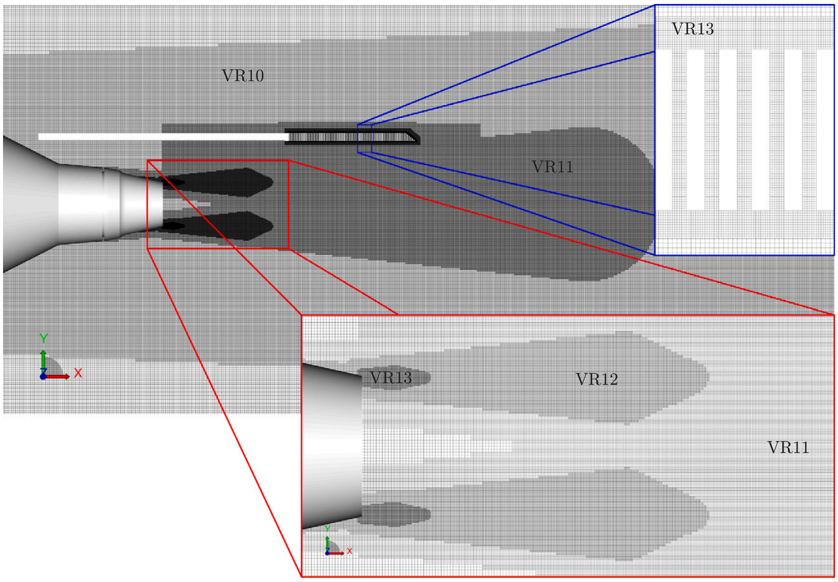

Fig. 7. Mesh at the symmetry plane of the installed jet set-up with a flat plate with perforated trailing edge. The finest element size for the medium resolution is 0.14 mm (VR13). This level of refinement is placed downstream of the nozzle lip and in the porous material. The following VR levels indicate a doubling in element size.

voxels/D_j), medium (resolution = 45 voxels/D_j), and fine (resolution = 64 voxels/D_j). The features of each grid are summarized in Table 5 for the installed jet with a metal foam trailing edge case (PM–APM formulation).

An image of the medium resolution mesh at the symmetry plane of the geometry ($z = 0$) is shown in Fig. 7 for the perforated trailing-edge case, which has the smallest channels. The different levels of grid refinement are defined by virtual volumes known as variable resolution (VR) regions. In total, 13 VRs are applied for the installed jet set-up, with the finest element (VR13) placed at the nozzle lip and in the permeable materials. For this resolution, the finest element size is 0.141 mm, as reported in Table 5. For each higher level of VR, the element size doubles. As shown in Fig. 7, the lipline region directly downstream of the nozzle exit is refined (VR13 and VR12) in order to properly capture the early stages of the shear layer formation. The remainder of the jet flow up to $x = 10D_j$ is included in VR11, whereas VR10 is the region comprised by FWH surface. With the medium grid resolution, a $y^+ = 70$ is computed at the nozzle exit. At the trailing edge, since there is no steady flow around the flat plate, it is not possible to extract a y^+ value.

The installed jet set-up with a fully solid plate has been previously validated by Rego et al. [51] both in terms of steady flow field and acoustics. It is also necessary to validate the unsteady properties of the jet flow, which are important for the analyzes in this work, against experimental data. For that purpose, the unsteady pressure is computed for the isolated case at $x = 6D_j - y = 1.5D_j$ (trailing-edge position in the installed case) with $M_a = 0.5$ and medium grid resolution, and compared with microphone measurements performed in the campaign described in [13]. The spectra are shown in Fig. 8 in terms of Power Spectral Density (PSD) versus Strouhal number ($St = f \times D_j/U_j$). A reference pressure of 2×10^{-5} Pa is used for the conversion to dB.

The spectra show good agreement in the low-frequency range, up to $St = 0.4$ with maximum deviations of approximately 2 dB/Hz. For $St > 0.4$, which is in the inertial subrange/acoustic field for this position as shown by the sharp decay in the spectrum, there are differences on the order of 4 dB/Hz. However, this frequency range is not of particular interest for jet-installation effects nor the noise reduction provided by the permeable materials, based on the results of Rego et al. [13], which are concentrated in the energy-containing region of the spectrum ($St < 0.3$).

A grid convergence study and set-up validation are also carried out in terms of far-field spectra for the cases with flow-permeable trailing-edges. The effect of grid resolution is assessed for the configuration with a metal foam trailing edge, as shown in Fig. 9(a), for a $M_a = 0.5$ jet. The spectra are obtained for a polar angle $\theta = 90°$ (reflected side) and are plotted in terms of Sound Pressure Level (SPL), for a constant frequency band of 100 Hz. The spectra are also compared with experimental results from Rego et al. [13]

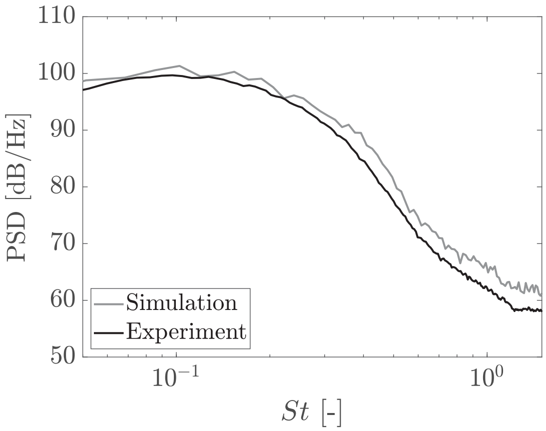

Fig. 8. Near-field pressure spectra computed at $x = 6D_j - y = 1.5D_j$ for the isolated jet at $M_a = 0.5$ and compared with experimental microphone measurements [13].

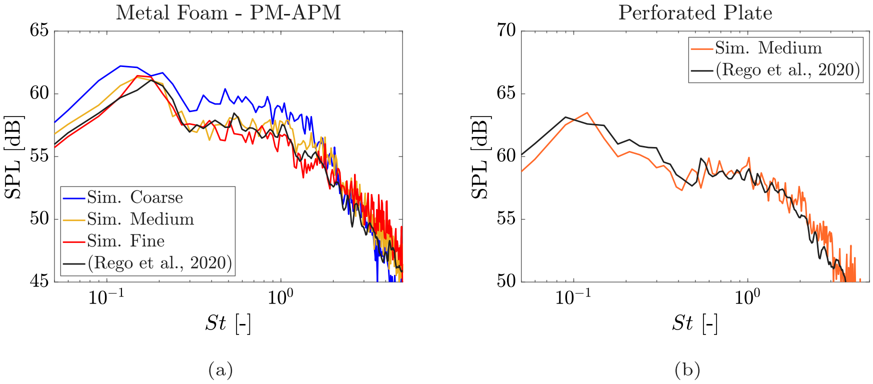

Fig. 9. Grid convergence analysis and validation. Far-field spectra of the installed jet with a (a) Metal foam trailing edge for different grid resolutions, compared to experimental results [13]. (b) Perforated trailing edge at medium grid resolution, compared to experimental results [13]. Spectra obtained at $\theta = 90°$ and for $M_a = 0.5$.

for set-up validation. The frequency band of the experimental data has been changed to 100 Hz, so that it is comparable with the computational results.

As shown in Fig. 9(a), the spectral shape is correctly predicted by the simulations from all grids. The curve for the coarse mesh has a slightly higher amplitude up to $St = 2$, indicating that smaller flow structures are not accurately resolved, and consequently their energy content is included in that frequency range. For $St > 2$, there is a sharp decay in amplitude due to the grid cut-off size. The spectra for the medium and fine grids, on the other hand, display similar amplitudes, within 1 dB variation, indicating grid convergence. There is also a good agreement with the experimental results from Rego et al. [13], with maximum deviations on the order of 1.5 dB, indicating that the PM–APM approach for the modeling of the metal foam is valid along with the prescribed resistivity inputs. The computational set-up is also validated for when the actual flow-permeable geometry is used in the simulations. The spectrum for the perforated plate case, computed at $\theta = 90°$ and for the medium resolution, is compared with experimental results of Rego et al. [13], as shown on Fig. 9(b). Similarly as the metal foam, there is a good agreement between the simulation and experiment, with a correct predicted spectral shape, and a maximum deviation of 2 dB. Therefore, the analyzes carried out in the remainder of this paper are obtained for a medium resolution grid, which is shown to predict accurate results with a relatively low computational cost.

4. Results and discussion

4.1. Jet flow field

The jet flow field is described in this section. A contour of the time-averaged velocity field for the installed jet at $M_a = 0.5$ (condition 2) is shown in Fig. 10. The region corresponding to the potential core and the downstream velocity decay are visible, as well as the spreading of the jet and symmetry with respect to the centerline. There is also no grazing flow occurring on the surface, and thus the jet development is not affected by the plate [13].

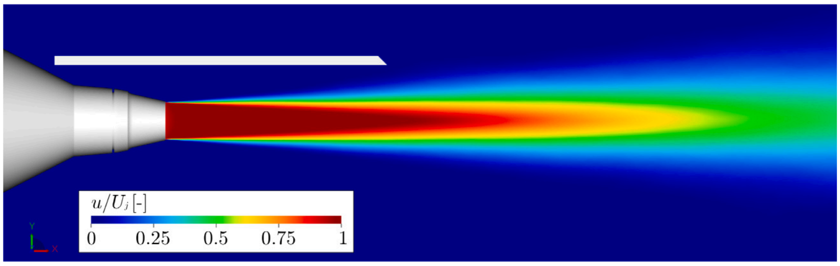

Fig. 10. Contour of time-averaged axial velocity u for the installed jet at condition 2 ($M_a = 0.5$), non-dimensionalized by the jet nominal velocity U_j.

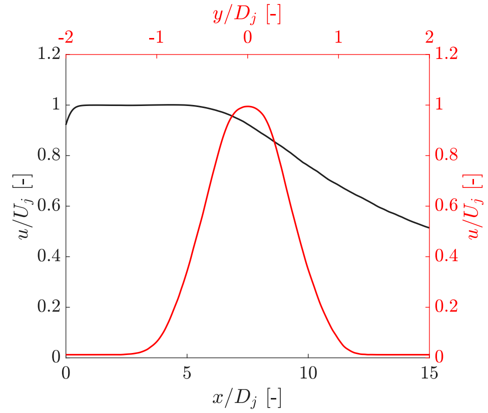

Fig. 11. Time-averaged axial velocity profiles for the installed jet at condition 2 ($M_a = 0.5$). Black curve — centerline velocity ($y = 0$). Red curve — radial profile at $x = 6D_j$. (For interpretation of the references to color in this figure legend, the reader is referred to the web version of this article.)

The time-averaged velocity profile is extracted at the jet centerline ($y = 0$) and plotted as the black curve in Fig. 11. The potential core length, defined as the distance between the position where $u = 0.98U_j$ and the nozzle exit plane, is found to be $6.2D_j$. Downstream of this position, the centerline velocity decay is visible. The velocity profile in the radial direction is also plotted in Fig. 11 (red curve), for $x = 6D_j$ (equivalent to the trailing edge position). The axial velocity reaches the free-stream level of $0.01U_j$ at a position $y \approx 1.2D_j$, and thus it is confirmed that there is no steady jet flow grazing on the surface. The spreading angle of the jet is also computed as $\delta = 8.5°$, which is consistent for the investigated nozzle geometry [52]. Similar results are obtained for the jet at $M_a = 0.3$.

4.2. Far-field noise spectra

In this section, the far-field SPL for the installed jet with flow-permeable trailing-edges are reported and compared to the reference solid configuration and the isolated jet. The spectra are obtained for a constant frequency band of 100 Hz, at a polar angle $\theta = 90°$ (reflected side), and plotted in Fig. 12 for both jet conditions.

Comparing initially the results for the isolated jet and the installed case with the solid plate, it is shown that installation effects result in a low-frequency noise amplification; the maximum increase with respect to the isolated case is 21 dB at $St = 0.15$ ($M_a = 0.3$), and 17 dB at $St = 0.12$ ($M_a = 0.5$). For the latter, with a higher jet velocity, the quadrupole sources due to turbulent mixing become more acoustically efficient with respect to the dipoles on the plate, and thus the relative low-frequency noise amplification due to installation effects is lower. At mid and high frequencies ($St > 0.6$ for $M_a = 0.3$ and $St > 0.4$ for $M_a = 0.5$), there is a constant offset between the installed and isolated spectra of approximately 3 dB due to reflection of acoustic waves from quadrupole sources [10].

The configurations with flow-permeable trailing edges show significant noise reduction with respect to the reference solid case, particularly for $St < 0.4$, where installation effects are dominant. For $M_a = 0.3$, reductions of 10 dB are obtained at the spectral peak ($St = 0.15$) for the metal foam and diamond trailing edges, whereas the perforated provides 7 dB reduction. For frequencies higher than the spectral peak, the noise levels of all flow-permeable configurations become similar. Similar trends occur for $M_a = 0.5$, with amplitude reductions of 12 dB (metal foam and diamond) and 9 dB (perforated), with respect to the solid case, at the spectral peak ($St = 0.12$). The metal foam and diamond display similar amplitude, except at very low frequencies ($St < 0.1$), for which the latter performs better. For the higher jet velocity, the noise levels of the flow-permeable trailing-edge configurations are closer to the isolated one, which is in agreement with the results from Rego et al. [13].

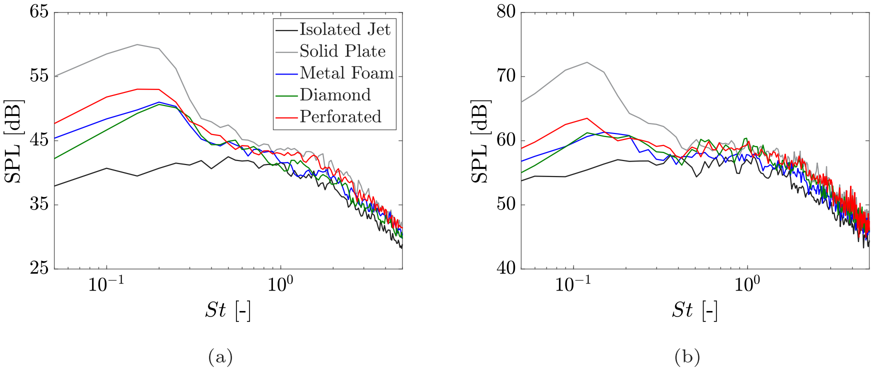

Fig. 12. Far-field spectra for the flow-permeable trailing edge configurations, compared with isolated jet and the reference solid case, for $\theta = 90°$ (a) $M_a = 0.3$. (b) $M_a = 0.5$.

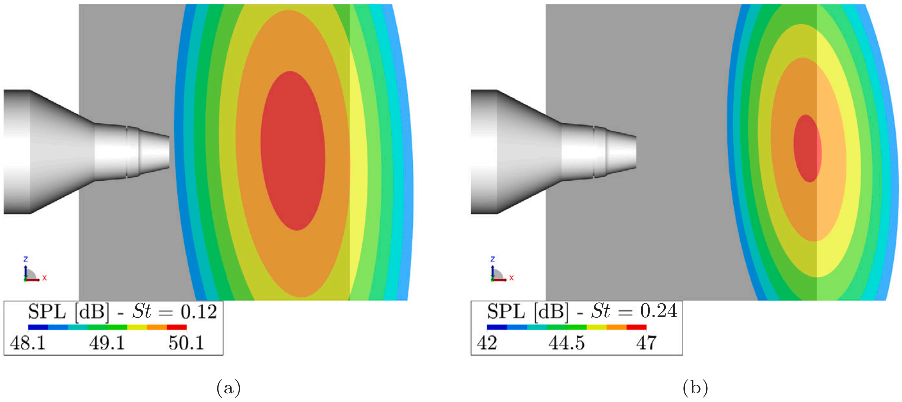

Fig. 13. Acoustic source location from beamforming applied to the installed jet with a fully solid plate ($M_a = 0.5$). (a) $St = 0.12$. (b) $St = 0.24$.

4.3. Far-field noise breakdown

Despite the visible reduction in SPL amplitude due to the permeable trailing edges, the dominant sources for those configurations are not yet clear. Rego et al. [13] hypothesized that the noise at the original trailing edge is largely reduced, and the junction becomes a region of strong acoustic scattering and possibly the dominant source for the permeable cases. In order to verify this hypothesis, the beamforming technique is applied to study the location of the dominant acoustic source, as described in Section 3.3. The results are evaluated for a scan plane on the lower side of the plate, initially for the fully solid case as a baseline, at $St = 0.12$ (far-field spectral peak) and $St = 0.24$, as shown in Fig. 13, for the $M_a = 0.5$ jet. Similar results are obtained for the other condition.

The contour plot in Fig. 13(a) shows that, for a frequency $St = 0.12$, the dominant acoustic source on the lower side of the plate is placed upstream of the trailing-edge, centered at $x = 4.1D_j$. On the other hand, for $St = 0.24$, the source is located at the trailing edge. Therefore, the results indicate that for $St = 0.12$ the unsteady loading due to surface pressure fluctuations is the dominant mechanism, whereas for $St = 0.24$ the scattering at the edge is more significant. Results for intermediate frequencies ($0.12 < St < 0.24$), not displayed for the sake of brevity, show that the source progressively moves towards the trailing edge, as the frequency is increased. The contours also show that the SPL for the source at $St = 0.12$ is higher than for $St = 0.24$, in agreement with the far-field spectra. The discussion on the dominant noise generation mechanisms on the noise spectra will be addressed in Section 4.5.

Source localization is also applied to the flow-permeable configurations. The results are shown in the contour plots of Fig. 14, for the $M_a = 0.5$ jet and $St = 0.12$. Different color scales are used for each configuration in order to facilitate the visualization. For the metal foam and diamond trailing edges, the dominant acoustic source at a frequency $St = 0.12$ is located near the junction between the solid and flow-permeable regions of the plate ($x = 3D_j$). For those configurations, this region acts as a geometric discontinuity and, therefore, it is also a scattering region for hydrodynamic waves in the jet mixing layer. In the junction, it is also expected that the sound field is governed by diffraction effects, for which some of the energy present in near-field hydrodynamic fluctuations in the jet mixing layer is converted into acoustic waves at the edge [6]. For the perforated case, a behavior similar to that of the original solid case is obtained, with the source upstream of the trailing edge ($x = 4.6D_j$), but downstream of the junction.

Since the junction has become the dominant source location for the metal foam and diamond configurations, it is useful to compare the noise generated by the solid ($x < 3D_j$) and porous ($x > 3D_j$) regions of the plate separately. For that purpose, the

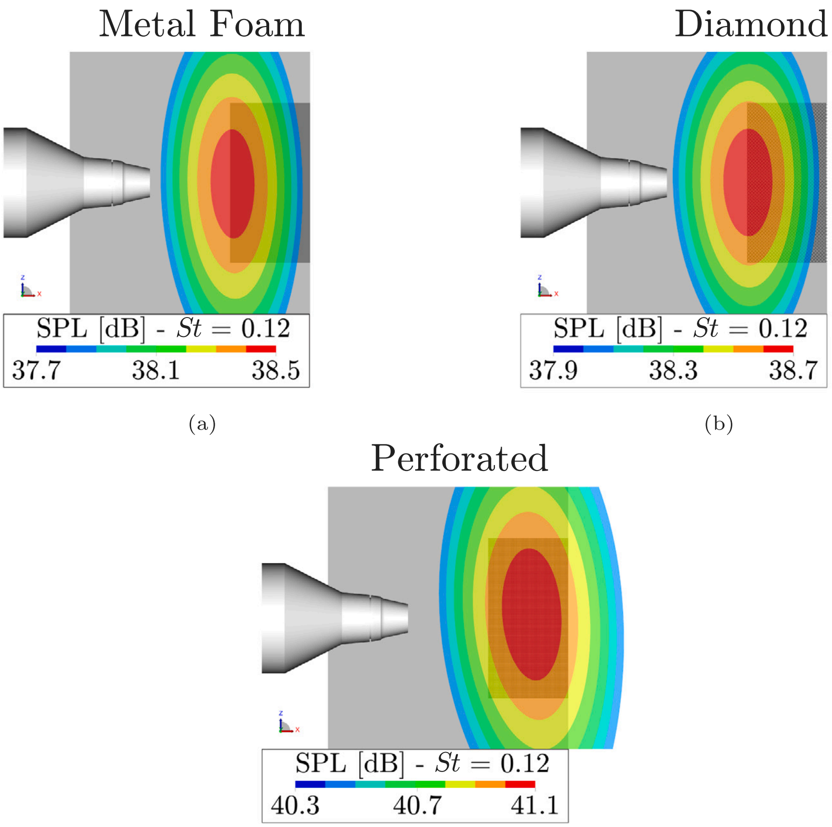

(a)

(b)

(c)

Fig. 14. Acoustic source location from beamforming applied to the installed jet with flow-permeable trailing edges, for a frequency $St = 0.12$ and $M_a = 0.5$. (a) Metal foam. (b) Diamond. (c) Perforated. (For interpretation of the references to color in this figure legend, the reader is referred to the web version of this article.)

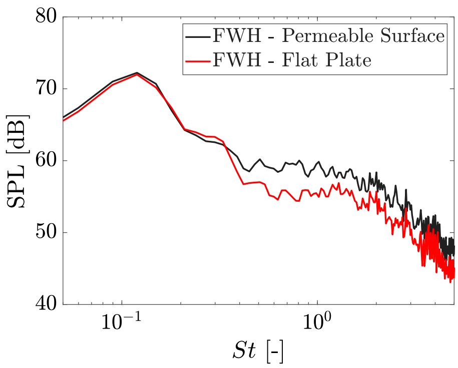

Fig. 15. Far-field SPL spectra for the installed jet with a fully solid plate, obtained from the FWH analogy applied to different surfaces: a permeable cylinder encompassing the whole geometry (black curve) and considering just the fluctuations on the flat plate surface (red curve). Spectra obtained for $\theta = 90°$ and $M_a = 0.5$. (For interpretation of the references to color in this figure legend, the reader is referred to the web version of this article.)

far-field noise produced by pressure fluctuations on the plate is computed through the FWH analogy [31] applied to those surfaces. However, it is necessary first to verify that this approach provides correct results, as well as confirm that the computed noise due to jet-installation is independent of the chosen FWH surface. Therefore, the spectra shown in Fig. 15 are obtained for the fully solid plate case from fluctuations on the permeable FWH surface encompassing the whole geometry, as well as those on the flat plate surfaces (upper and lower sides, leading edge and trailing edge). The spectra are obtained for a polar angle $\theta = 90°$ and $M_a = 0.5$. The black curve is the same as the solid plate spectrum of Fig. 12(b).

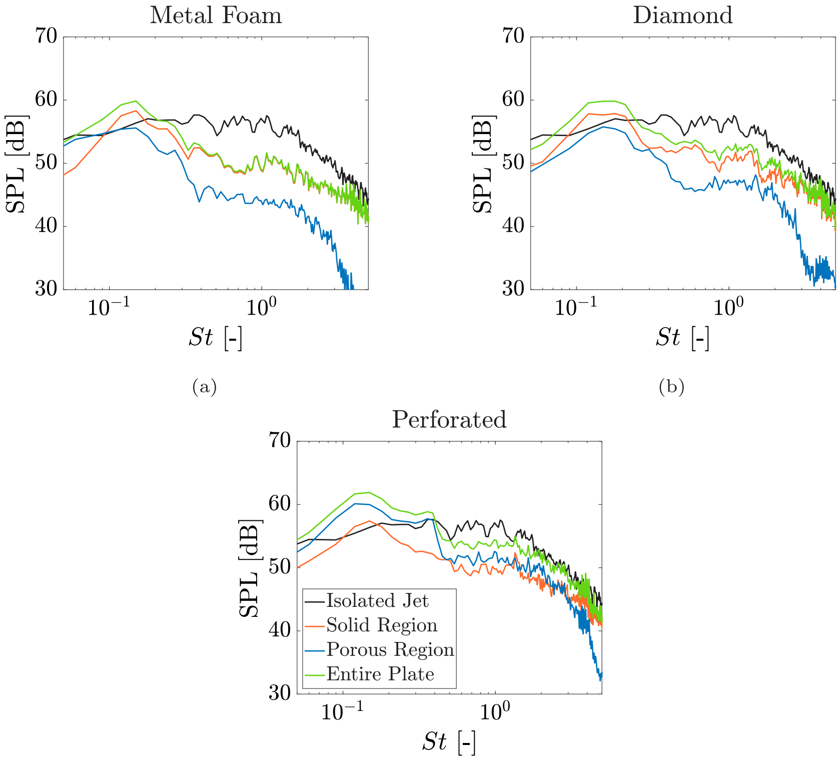

(a) (b)

(c)

Fig. 16. Far-field noise spectra generated by solid (orange curve) and porous (blue curve) regions of the plate separately, for each flow-permeable configuration and $M_a = 0.5$. The solid section of the plate extends up to $x = 3D_j$, whereas the permeable one is located at $3D_j < x < 6D_j$. The green curve represents the noise generated by the entire plate (sum of solid and porous regions). (a) Metal foam. (b) Diamond. (c) Perforated. (For interpretation of the references to color in this figure legend, the reader is referred to the web version of this article.)

There is a good agreement between the curves up to $St = 0.3$, which is the frequency range where jet-installation noise is dominant. This shows that the noise levels are accurately predicted and independent of the chosen FWH surface. At higher frequencies, the curves do not agree since the spectrum obtained from the flat plate pressure fluctuations does not properly capture the quadrupole sources in the jet mixing layer. However, this frequency range is not relevant for the current analysis.

For the permeable trailing edge cases, the spectra are computed individually for each region of the plate, i.e. solid (orange curve) and porous (blue curve), as plotted in Fig. 16, for $\theta = 90°$ and $M_a = 0.5$. The isolated jet spectrum is also included for reference, as well as the noise generated by the entire plate (green curve), which is equivalent to the sum of the solid and porous regions.

For the metal foam, the spectra show that the noise generated by the solid region of the plate is dominant with respect to the porous part, except for low frequencies up to $St = 0.09$. For the diamond configuration, the solid region of the plate is dominant in the entire analyzed frequency range. The perforated case, on the other hand, displays the opposite behavior: the porous region has a higher amplitude than the solid one, even up to high frequencies ($St = 1.3$). These results are in agreement with the dominant acoustic source position obtained from beamforming, as shown in Fig. 14. Moreover, considering the noise generated by the entire plate for each configuration (green curves), it is visible that for the metal foam and diamond cases, the amplitude is approximately of the same order as the isolated jet. It is also interesting to notice that, for the metal foam, the frequency range where the porous section generates more noise than the solid one ($St \leq 0.09$) is the same range as in the spectra of Fig. 12 where the noise for the metal foam configuration is higher than that of the diamond. Therefore, this difference occurs because more noise is generated by the porous region of the plate, so it is likely due to the different material properties. This is verified in the next section.

4.4. Volumetric flow rate and surface pressure distribution

In this section, the difference between the far-field noise levels of the permeable configurations is linked to the properties of each material, particularly the resistivity, which, according to Darcy's law, affects directly the pressure drop across the surface. In order to verify this hypothesis, the Root-Mean-Square (RMS) volumetric flow rate, integrated through the permeable region of the plate, is computed and reported in Table 6, for both jet conditions. The values are non-dimensionalized by the nominal jet volumetric flow rate for each condition ($U_j \times \pi D_j^2/4$). The flow rate through an equivalent virtual surface, with the same dimensions as the permeable trailing edges ($3D_j < x < 6D_j$, $y = 1.5D_j$ and $-3D_j < z < 3D_j$), is also computed for the isolated jet. This surface simply

Table 6
Root-mean-square volumetric flow rate through the porous region for each flow-permeable configuration, non-dimensionalized by the nominal jet mass flow of each condition. The flow rate through an equivalent surface is also computed for the isolated jet as a reference value.

M_a [–]	$\dot{m}_{\text{isolated}}$ [10^{-3}]	$\dot{m}_{\text{metal foam}}$ [10^{-3}]	$\dot{m}_{\text{diamond}}$ [10^{-3}]	$\dot{m}_{\text{perforated}}$ [10^{-3}]
0.3	7.32	6.09	6.87	4.42
0.5	7.98	7.13	7.54	4.77

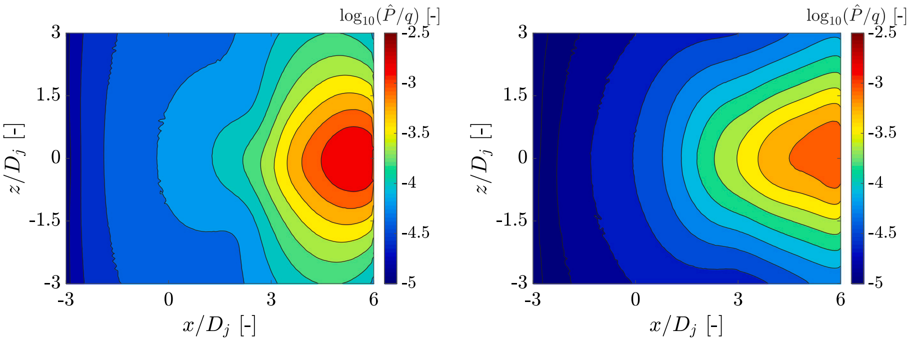

(a) (b)

Fig. 17. Pressure distribution on the lower side of the plate, for a frequency $St = 0.12$ and $M_a = 0.5$. (a) Fully solid plate. (b) Metal foam trailing edge.

consists of a measurement plane in the isolated jet, parallel to the lower side of the plate surface in the installed case and does not affect the flow development. Regarding the volumetric flow rate, the extreme cases are the isolated jet, for which there is no flow blockage, and the installed case with solid plate, for which there is total blockage and zero flow rate through the surface. The goal of the analysis is then to define where each permeable case is located with respect to those two extremes and link the findings to the properties of the material (porosity and permeability) and the surface pressure fluctuations which are directly correlated to the produced noise.

The results show that the non-dimensionalized values are similar for both conditions, indicating that the flow velocity through the porous material is likely proportional to the jet velocity. Moreover, comparing the different configurations, the diamond and metal foam have similar volumetric flow rates, both higher than that of the perforated. Therefore, the latter provides higher blockage to the unsteady flow normal to the plate surface. The flow rates through the metal foam and diamond trailing edges are also close to the reference value of the isolated jet, indicating that a further increase in the structure permeability is not likely to result in significant changes to the flow rate, and possibly no change to the noise levels.

The unsteady flow through the permeable trailing edge affects the pressure balance across the surface, which is directly responsible for the noise generation. Therefore, the distribution of pressure fluctuations $\hat{P}$ on the surface, in the frequency domain, is analyzed for each flow-permeable configuration and compared with the reference solid case. Firstly, contour plots of the pressure on the lower side of the plate are shown in Fig. 17 in logarithmic scale, for a frequency $St = 0.12$, and for the solid and metal foam cases respectively. The other flow-permeable cases display similar trends as the metal foam. The values are non-dimensionalized by the nominal jet dynamic pressure ($0.5\rho U_j^2$). It is worth mentioning that these plots also consider pressure fluctuations of hydrodynamic characteristic and, therefore, they are not necessarily equivalent to acoustic source maps.

The maximum amplitude of pressure fluctuations for the metal foam is visibly lower than for the reference solid case because of the flow through the porous material. Since there is communication between the upper and lower sides of the plate near the trailing edge, the unsteady flow generated by the jet mixing layer is no longer bounded by the surface at this region, and the consequent vertical velocity component through the permeable material leads to a reduction of the surface static pressure.

In more detail, the pressure distribution in the streamwise direction of the plate, in the symmetry plane ($z = 0$), is plotted in Fig. 18(a). It is shown that the amplitude of pressure fluctuations for the cases with flow-permeable trailing edges is lower than that of the solid case, except for the region around $x = 3D_j$. This point corresponds to the solid–porous junction of the plate, which acts as a scattering region. This behavior is present for the metal foam and diamond cases, and confirmed by the beamforming results of Fig. 14. Moreover, the amplitude near the trailing edge is lower for all flow-permeable cases with respect to the solid one and the trend is consistent with the volumetric flow rate through each configuration. The metal foam only differs from the diamond close to the trailing-edge position. Finally, near the nozzle exit ($x < 1.5D_j$), the jet has not yet developed sufficiently in order to generate strong hydrodynamic pressure fluctuations. This effect, coupled with a nearly constant amplitude up to $x = 1.5D_j$ for the solid case, suggests that the pressure fluctuations in this region are dominated by acoustic waves scattered at the plate trailing edge. These acoustic waves have a dipole/cardioid directivity pattern and thus travel upstream of the trailing edge. For the permeable cases, there is a consistent increase in amplitude moving downstream, indicating that the scattered acoustic waves are weaker than the linear hydrodynamic field of the jet. Therefore, the difference between the solid and permeable cases in this region is linked to a weaker scattering mechanism for the permeable cases.

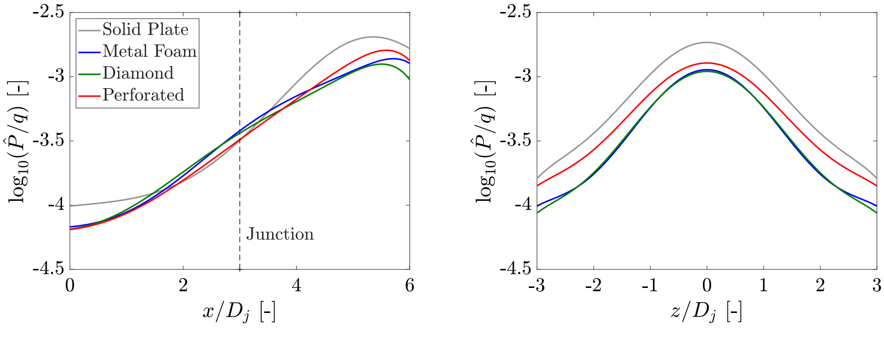

(a) (b)

Fig. 18. Amplitude of pressure fluctuations on the lower side of the plate, for a frequency $St = 0.12$ and $M_a = 0.5$ (a) Streamwise direction at $z = 0$. (b) Spanwise direction at $x = 5D_j$.

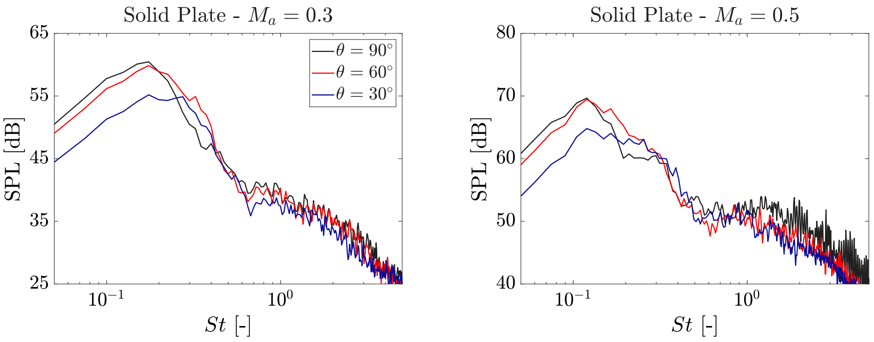

(a) (b)

Fig. 19. Far-field spectra of the surface pressure fluctuations for the installed jet (solid plate) at different polar angles. (a) $M_a = 0.3$. (b) $M_a = 0.5$.

A similar analysis is also carried out in the spanwise direction of the plate, at a fixed streamwise position $x = 5D_j$, as shown in Fig. 18(b). At this position, the amplitude of pressure fluctuations for the flow-permeable cases is lower than that of the solid case throughout the entire span of the porous region. The metal foam and diamond curves practically collapse, whereas the perforated has higher amplitude, particularly at $z = \pm 3D_j$. This is likely due to a misalignment between the unsteady flow from the jet (always in the radial direction) and the axis of the holes in the perforation, leading to a reduced volumetric flow rate far from the centerline. However, the amplitude of fluctuations at that region is almost one order of magnitude lower than at the centerline. Since the trailing edge is located in the linear hydrodynamic field of the jet [51], where the pressure decays exponentially with radial distance from the shear layer, the center of the plate ($z = 0$) is subjected to impingement of stronger pressure fluctuations with respect to the spanwise extremities of the permeable materials ($z = \pm 3D_j$). Therefore, it is expected that the difference between the permeable cases near $z = \pm 3D_j$ does not have a significant contribution to the far-field noise.

4.5. Noise from pressure wave impingement and trailing-edge scattering

The results in the previous section have shown how the permeable trailing edges modify the flow around the plate with consequent changes to the surface pressure distribution. However, it is still necessary to assess how the noise generation mechanisms on the solid plate, i.e. the impingement of pressure waves on the surface and the scattering at the edge, are individually affected by the permeable trailing edges. The main distinction between these mechanisms is their directivity pattern (dipole and cardioid shapes, respectively). Therefore, in order to determine the conditions and frequency range where each of them is dominant, far-field spectra are plotted for three polar angles ($\theta = 30°$, $\theta = 60°$ and $\theta = 90°$), initially for the solid plate case, as shown in Fig. 19. These spectra are obtained solely from the pressure fluctuations on the surface in order to disregard noise from turbulence mixing. Moreover, these spectra are computed for a constant frequency band of 50 Hz so that a more accurate analysis in frequency is carried out.

As shown in Fig. 19, the far-field spectra of surface pressure fluctuations for $\theta = 90°$ have similar shape and amplitude as those shown in Fig. 12 for the installed jet with a fully solid plate, particularly at low and mid frequencies. However, for $\theta = 60°$, the spectral shape changes: for $M_a = 0.3$, the amplitude decreases slightly for $St < 0.2$, but increases for $0.2 < St < 0.4$, with respect to $\theta = 90°$. For $\theta = 30°$, the amplitude is mostly lower than that for $\theta = 90°$, except in the frequency range $0.28 < St < 0.4$. A similar trend occurs for $M_a = 0.5$.

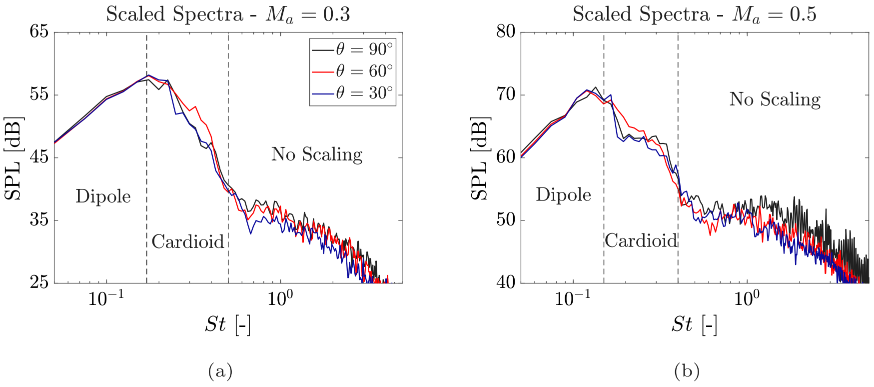

Fig. 20. Far-field spectra of the surface pressure fluctuations for the installed jet (solid plate) at different polar angles, scaled with a dipole directivity ($\sin^2(\theta)$) at low frequencies, and a cardioid ($\cos^2(\theta/2)$) at mid frequencies. (a) $M_a = 0.3$. (b) $M_a = 0.5$.

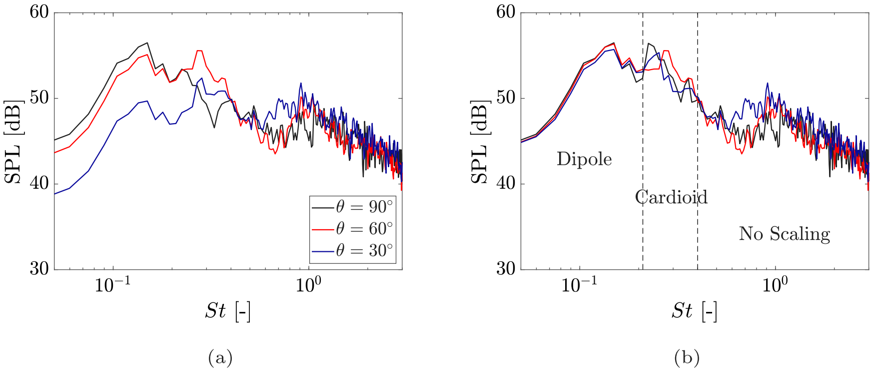

Fig. 21. Far-field noise generated by the solid region of the surface ($x < 3D_j$) with a metal foam trailing edge for $M_a = 0.5$. (a) SPL spectra for different polar angles. (b) Scaled SPL spectra based on dipole/cardioid directivity.

The low-frequency noise reduction with a decrease in polar angle can be associated with a dipolar directivity pattern, which has a maximum at the direction normal to the surface ($\theta = 90°$). As a consequence, the dominant noise generation mechanism in that frequency range is the unsteady loading on the plate due to the impingement of pressure waves. On the other hand, for the frequency range where there is an increase in amplitude with respect to $\theta = 90°$, the dominant noise mechanism is the scattering of hydrodynamic pressure waves at the trailing-edge, which has a cardioid directivity. However, for the latter, it would be expected that the curve for $\theta = 30°$ had an even higher amplitude than $\theta = 60°$, which is not the case. It is believed that this results from a combination of both mechanisms in the latter case, for which the noise produced by them have similar amplitude.

In order to verify that the far-field spectra has different dominant noise mechanisms at different frequencies, the curves for each polar angle can be scaled with a directivity characteristic of a dipole ($\sin^2(\theta)$) and a cardioid ($\cos^2(\theta/2)$), according to the polar angle convention. For each jet condition, the dipole scaling is applied to low frequencies, up to the spectral peak, whereas the cardioid scaling is applied to mid frequencies, starting at the peak up to the frequency where installation effects are dominant with respect to turbulence mixing. The scaled spectra are shown in Fig. 20, with the annotated scaling applied to each frequency range. A good agreement is obtained between the curves, particularly in the dipole region and around the spectral peak. The collapsing of the spectra are, therefore, an indication that the different noise generation mechanisms in an installed jet are dominant at different frequency ranges. Moreover, the small differences for the $\theta = 60°$ scaled curve at mid frequencies suggest that, for this case, the dipole effects are still considerable in this frequency range.

With the far-field spectrum of an installed jet with a fully solid plate properly characterized in terms of the dominant mechanisms at different frequencies, the effect of a permeable trailing edge on JIN can be properly addressed by linking the final noise signature to each noise generation mechanism. Spectra at different polar angles are obtained for the solid and porous regions of the plate separately. For the former, there are no significant differences between the results of different configurations. Therefore, the far-field spectra from the solid region ($x < 3D_j$) for the configuration with the metal foam trailing edge is shown in Fig. 21(a).

The spectra shown in Fig. 21(a) have a similar trend as those in Fig. 19 for the fully solid plate; at low frequencies the amplitude tends to decrease for shallow polar angles, whereas it increases with θ for mid frequencies. Therefore, a scaling based on dipolar/cardioid directivity can be applied to these spectra at different frequency ranges. The best agreement is found, when a dipole scaling is applied up to $St = 0.21$, and a cardioid one for $0.21 < St < 0.4$. Therefore, for this case, the scaling regions are not

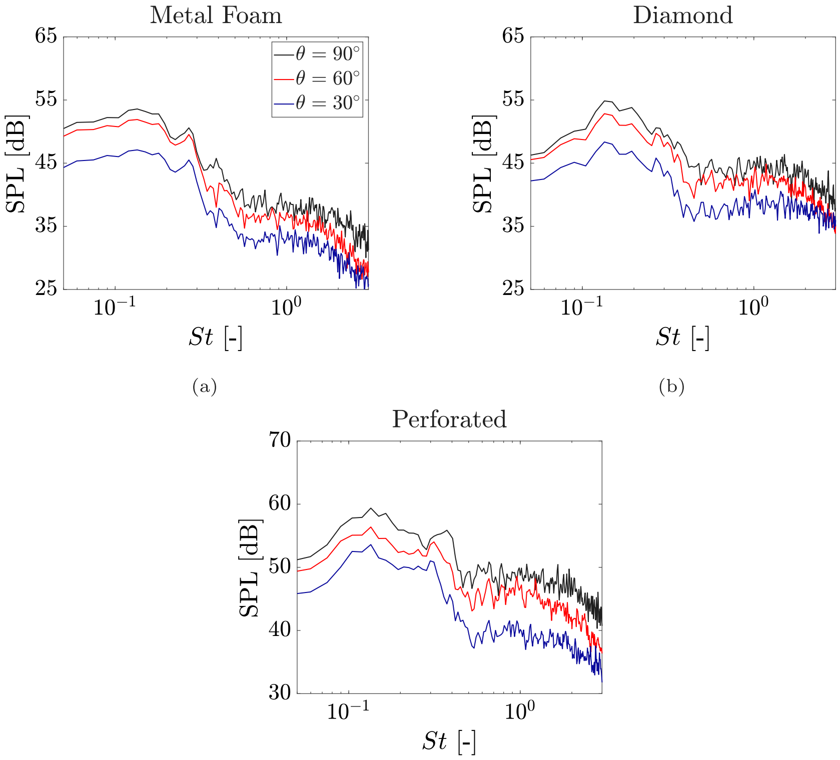

(a)

(b)

(c)

Fig. 22. Far-field noise generated by the porous region of the surface ($3D_j < x < 6D_j$), for different polar angles and $M_a = 0.5$. (a) Metal foam. (b) Diamond. (c) Perforated.

related to the spectral peak. The maximum frequency for dipole scaling is higher than that obtained from the original solid plate ($St = 0.12$) in Section 4.2. This is due to the position of the new geometric discontinuity (solid–porous junction), at $x = 3D_j$; at this point, the energy content of large-scale structures is lower than at the original trailing-edge position ($x = 6D_j$). Therefore, the contribution due to scattering at low frequencies is reduced, and thus a wider frequency range is dominated by dipole sources. It is also possible that the scattering efficiency at the junction is lower since the change of surface impedance from solid–porous is less abrupt than that from solid-air, as in the original solid case. Further research into this hypothesis is necessary.

For the permeable region of the plate ($3D_j < x < 6D_j$), the spectra for all configurations are shown in Fig. 22. The spectra display a similar trend: the SPL decreases with decreasing θ for the entire assessed frequency range. These results indicate that the dominant noise generation mechanism in the porous region is the unsteady loading due to pressure wave impingement. In order to confirm this assumption, a dipole directivity scaling is applied to the curves up to $St = 0.4$. The results in Fig. 23 show that a good agreement is obtained with the scaled spectra, confirming the mechanism responsible for noise generation for those cases. The absence of a frequency range with cardioid directivity indicates that the scattering mechanism is largely reduced at the original trailing-edge position. These results are in qualitative agreement with those from Jaworski and Peake [17], who demonstrated that the far-field noise at low frequencies, caused by edge scattering, changes from a fifth-power scaling with the flow velocity to a sixth-power one when the trailing edge is replaced by a permeable structure. This means that the far-field noise is no longer dominated by edge scattering (U^5), but instead it has a dipole characteristic (U^6), which is also visible in the spectra of Fig. 23. It is necessary, however, to assess how the permeable trailing edges affect noise scattering in the near-field.

According to Amiet [53], one of the parameters that affect the scattered noise produced by turbulence convecting past a trailing edge is the spanwise correlation at that region. Therefore, it is interesting to assess how the flow-permeable trailing edges affect this parameter, with respect to the original solid case. The coherence γ between pressure signals in the spanwise direction at the trailing-edge region ($x = 6D_j$) is computed, using the signal at the symmetry plane ($z = 0$) as reference. The results are plotted in Fig. 24 for a frequency $St = 0.12$. It is shown that the spanwise coherence is highest for the solid trailing-edge case, which is related to the flow diverted to the spanwise direction by the solid boundary. The flow-permeable cases, however, display similar values throughout the span, indicating that the permeability of the insert or the shape of the channels do not play a significant role in this parameter. Therefore, it is concluded that the noise due to scattering at the plate trailing edge is decreased not only due to a lower amplitude of surface pressure fluctuations, but also due to a lower spanwise coherence, which is similar for all permeable configurations.

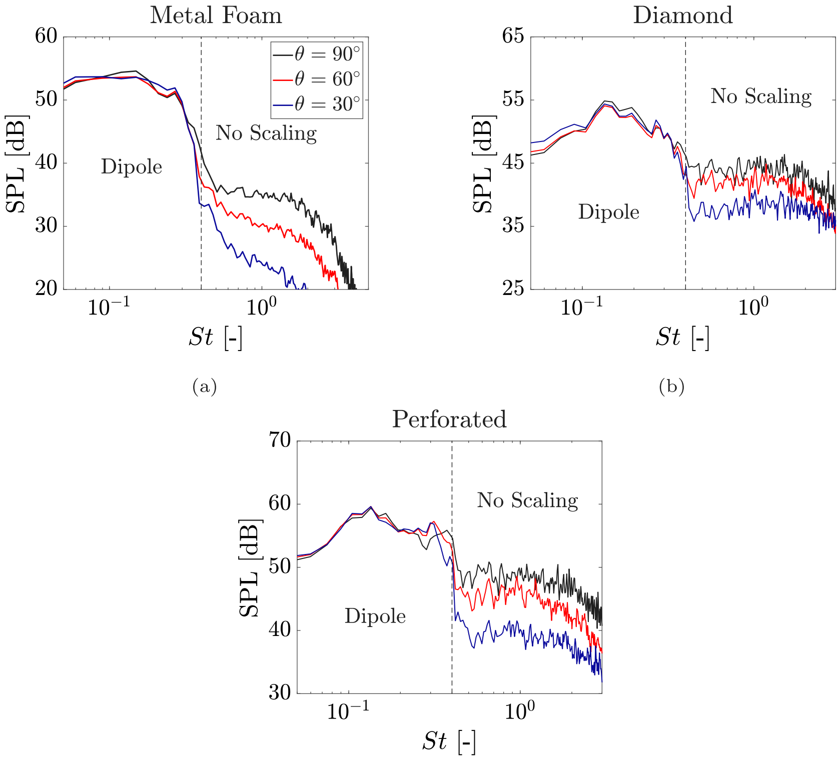

(a)

(b)

(c)

Fig. 23. Far-field noise generated by the porous region of the surface ($3D_j < x < 6D_j$), for different polar angles and $M_a = 0.5$. (a) Metal foam. (b) Diamond. (c) Perforated.

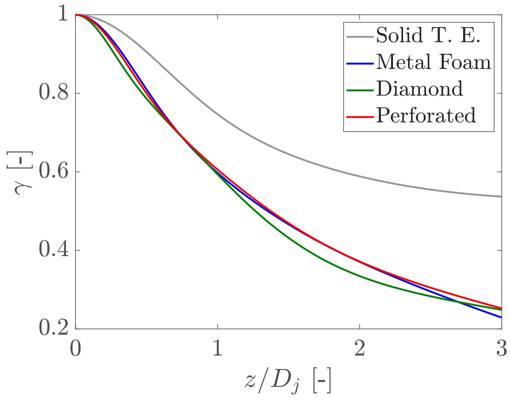

Fig. 24. Coherence values from surface pressure in the spanwise direction at the plate trailing edge ($x = 6D_j$), computed with the signal at the symmetry plane ($z = 0$) as reference for the solid and flow-permeable cases. Data plotted for $St = 0.12$ and $M_a = 0.5$.

As a confirmation that the noise due to scattering at the original trailing edge position is no longer dominant, the phase angle ϕ between the pressure fluctuations on the upper and lower sides of the plate is computed, at a position $x = 5D_j$, as plotted in Fig. 25(a). The results show a higher phase angle for the solid plate than those with permeable trailing edges. For the former, this phase difference is due to scattered acoustic waves traveling upstream, whereas for the latter, the lower phase shift is consistent with hydrodynamic fluctuations on both sides of the plate; acoustic waves scattered at the trailing edge are, therefore, considerably weaker in those cases. Moreover, the phase angle is also similar for all permeable cases, including the perforated plate, indicating that the insert resistivity is not affecting the phase of the pressure fluctuations traveling from the lower to the upper side of the plate. Combining these results with the spanwise coherence analysis, it is concluded that the reduction of noise due to edge scattering is independent of the trailing edge resistivity, for the investigated cases. Additionally, the lower amplitude of pressure fluctuations

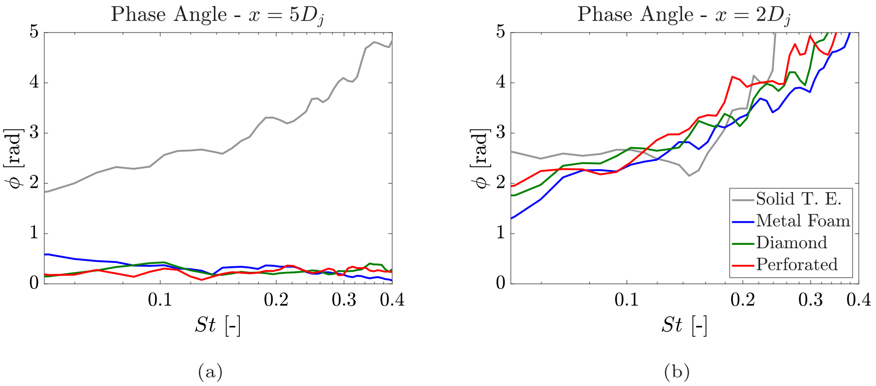

Fig. 25. Phase angle between pressure fluctuations on the lower and upper sides of the plate, computed for $M_a = 0.5$ at (a) $x = 5D_j$ and (b) $x = 2D_j$.

for the permeable cases with respect to the solid one near the nozzle exit, as shown in Fig. 18(a), is a direct consequence of lower noise due to scattering. Finally, the phase angle is also computed upstream of the junction, as shown Fig. 25(b). At this position, the phase shift is similar for the solid and permeable cases, indicating the effects of scattering at the solid–permeable junction.

Based on the obtained results, it is concluded that the scattering mechanism at the original trailing-edge position is no longer significant for the permeable configurations. This is valid for all types of inserts, thus showing how a structure with low permeability, such as the perforated, is still capable of providing considerable JIN reduction. The dominant noise generating mechanism in the permeable region is shown to be related to surface pressure fluctuations, which are intimately linked to the permeability/resistivity of the material, since these parameters define the flow rate through the permeable structure and, consequently, the amplitude of fluctuations. Considering the overall surface, this effect is summed to the noise produced by the solid region of the plate, generated both due to impingement of pressure waves as well as scattering at the solid–permeable junction, which is a new discontinuity introduced in the geometry.

5. Conclusions

A numerical investigation on jet-installation noise reduction with the application of permeable trailing edges is performed. The focus of this work consists in studying how those permeable structures provide noise reduction, by analyzing their effect on the main noise generation mechanisms of a plate in the vicinity of a jet, i.e. noise produced either by surface pressure fluctuations or trailing-edge scattering.

The model for the analyzes is comprised by a nozzle, generating a single-stream subsonic jet, and a flat plate placed in the linear hydrodynamic field with no grazing flow. The investigated permeable structures consist in a metal foam, which is modeled as an equivalent porous medium following Darcy's equation, due to its complex geometry. A perforated trailing edge, with straight holes normal to the jet axis, and a diamond-shaped structure are also investigated, but for these cases the actual geometry is simulated. The metal foam and diamond structures have a lower resistivity compared to perforated one. The permeable region of the plate has a length of $3D_j$ upstream of the trailing edge in the streamwise direction, and a $6D_j$ span.

Far-field results of the installed jet with a solid plate show a significant low-frequency noise increase with respect to the isolated configuration (17 dB at $St = 0.12$, for $M_a = 0.5$). By replacing the trailing-edge with a permeable structure, noise reduction of 12 dB are achieved at the spectral peak ($St = 0.12$ and $M_a = 0.5$) for the metal foam and diamond, whereas 9 dB reduction is obtained with the perforated structure. Beamforming results show that the dominant acoustic source is located at the solid–permeable junction for the metal foam and diamond cases, confirming the hypotheses from the literature, whereas for the perforated it is located on the insert, upstream of the original trailing edge, similarly as the solid case. It is shown that the pressure fluctuations on the perforated trailing edge are considerably higher than the other structures, for which most of the noise is generated by the solid section of the plate.

By analyzing far-field results for different polar angles, different behaviors are observed for the solid and permeable sections of the plate. The former exhibits the same characteristics as the original solid plate, with noise at low frequencies displaying a dipolar directivity and, at relatively higher frequencies, with a cardioid shape. This dual behavior is also verified through beamforming results. For the permeable region, on the other hand, the spectra display a consistent dipolar directivity throughout the entire frequency range where the installation effects are dominant. This occurs for all investigated permeable configurations, thus showing that the scattering mechanism at the original trailing-edge position is strongly reduced, even for the perforated case, which has a high resistivity. These results are confirmed by analyzing the spanwise coherence and the phase shift between the upper and lower sides of the plate. Therefore, noise due to scattering at the trailing edge is largely reduced for all permeable configurations, and the dominant mechanism in that region of the plate is the unsteady loading to pressure wave impingement.

Further work on this topic will focus on mitigating the effect of the solid–porous junction, which becomes a new discontinuity in the geometry and a region of significant noise generation. For this purpose, a gradual increase in permeability towards the trailing edge is likely to mitigate the generated noise. Moreover, the permeable structures should also be investigated in a realistic wing geometry, as well as with a free stream condition, for which the amplitude of fluctuations in the jet shear layer will be reduced due to a lower velocity difference between the jet and ambient. Consequently, jet-installation effects and the noise reduction provided by the porous materials will also be relatively lower. It is also expected that there will be penalties to the aerodynamic characteristics, such as lift reduction and drag increase, particularly if there is flow communication between the lower and upper sides of the wing. These, however, can be minimized by tailoring the properties of the permeable materials, while still providing sufficient noise reduction.

CRediT authorship contribution statement

Leandro Rego: Conceptualization, Methodology, Validation, Formal Analysis, Investigation, Data curation, Writing - original draft, Writing - review & editing, Visualization. **Francesco Avallone:** Writing - review & editing, Visualization, Supervision. **Daniele Ragni:** Writing - review & editing, Visualization, Supervision. **Damiano Casalino:** Writing - review & editing, Visualization, Supervision.

Acknowledgments

This work is part of the IPER-MAN project (Innovative PERmeable Materials for Airfoil Noise Reduction), project number 15452, funded by the Netherlands Organization for Scientific Research (NWO). The authors would like to thank Alejandro Rubio-Carpio and Christopher Teruna, for providing the parameters from the porous materials characterization. The authors would also like to thank Dr. Mirjam Snellen and Prof. Sybrand van der Zwaag from the Delft University of Technology, for collaboration in the project.

Declaration of competing interest

The authors declare that they have no known competing financial interests or personal relationships that could have appeared to influence the work reported in this paper.

References

[1] D.L. Huff, Noise reduction technologies for turbofan engines, NASA/TM—2007-214495 (2007) 1–17.
[2] M.J. Lighthill, On sound generated aerodynamically I. General theory, Proc. R. Soc. A 211 (1107) (1952) 564–587, http://dx.doi.org/10.1098/rspa.1952.0060.
[3] J.L.T. Lawrence, M. Azarpeyvand, R.H. Self, Interaction between a flat plate and a circular subsonic jet, in: 17th AIAA/CEAS Aeroacoustics Conference, Portland, OR, USA, 2011, http://dx.doi.org/10.2514/6.2011-2745.
[4] C. Brown, Jet-surface interaction test: Far-field noise results, in: Proceedings of the ASME Turbo Expo 2012: Power for Land, Sea and Air, Copenhagen, Denmark, 2012, pp. 1–13.
[5] N. Curle, The influence of solid boundaries upon aerodynamic sound, in: Proceedings of the Royal Society a 231, 1955, pp. 505–514, http://dx.doi.org/10.1098/rspa.1955.0191.
[6] J.E. Ffowcs-Williams, L.H. Hall, Aerodynamic sound generation by turbulent flow in the vicinity of a scattering half plane, J. Fluid Mech. 40 (4) (1970) 657–670, http://dx.doi.org/10.1017/S0022112070000368.
[7] M. Roger, S. Moreau, K. Kucukcoskun, On sound scattering by rigid edges and wedges in a flow, with applications to high-lift device aeroacoustics, J. Sound Vib. 362 (2016) 252–275, http://dx.doi.org/10.1016/j.jsv.2015.10.004.
[8] R.W. Head, M.J. Fisher, Jet/surface interaction noise - Analysis of farfield low frequency augmentations of jet noise due to the presence of a solid shield, in: 3rd AIAA Aeroacoustics Conference, Palo Alto, CA, USA, 1976, http://dx.doi.org/10.2514/6.1976-502.
[9] L. Rego, F. Avallone, D. Ragni, D. Casalino, Noise amplification effects due to jet-surface interaction, in: AIAA Scitech 2019 Forum, San Diego, CA, USA, 2019, http://dx.doi.org/10.2514/6.2019-0001.
[10] A.V.G. Cavalieri, P. Jordan, W.R. Wolf, Y. Gervais, Scattering of wavepackets by a flat plate in the vicinity of a turbulent jet, J. Sound Vib. 333 (24) (2014) 6516–6531, http://dx.doi.org/10.1016/j.jsv.2014.07.029.
[11] D. Papamoschou, Prediction of jet noise shielding, in: 48th AIAA Aerospace Sciences Meeting Including the New Horizons Forum and Aerospace Exposition, Orlando, FL, USA, 2010, http://dx.doi.org/10.2514/6.2010-653.
[12] D. Casalino, A. Hazir, Lattice Boltzmann based aeroacoustic simulation of turbofan noise installation effects, in: 23rd International Congress on Sound & Vibration, Athens, Greece, 2014, pp. 1–8.
[13] L. Rego, D. Ragni, F. Avallone, D. Casalino, R. Zamponi, C. Schram, Jet-installation noise reduction with flow-permeable materials, J. Sound Vib. 498 (2021) 115959, http://dx.doi.org/10.1016/j.jsv.2021.115959.
[14] J.D. Revell, H.L. Kuntz, F.J. Balena, B.L. Storms, R.P. Dougherty, Trailing-edge flap noise reduction by porous acoustic treatment, in: 3rd AIAA/CEAS Aeroacoustics Conference, Atlanta, GA, USA, 1997, http://dx.doi.org/10.2514/6.1997-1646.
[15] M. Herr, K. Rossignol, J. Delfs, N. Lippitz, M. Möß ner, Specification of porous materials for low-noise trailing-edge applications, in: 20th AIAA/CEAS Aeroacoustics Conference, Atlanta, GA, USA, 2014, http://dx.doi.org/10.2514/6.2014-3041.
[16] E. Sarradj, T. Geyer, Noise generation by porous airfoils, in: 13th AIAA/CEAS Aeroacoustics Conference, Rome, Italy, 2007, http://dx.doi.org/10.2514/6.2007-3719.
[17] J.W. Jaworski, N. Peake, Aerodynamic noise from a poroelastic edge with implications for the silent flight of owls, J. Fluid Mech. 723 (2013) 456–479, http://dx.doi.org/10.1017/jfm.2013.139.
[18] A. Rubio Carpio, R. Merino Martínez, F. Avallone, D. Ragni, M. Snellen, S. Van Der Zwaag, Broadband trailing edge noise reduction using permeable metal foams, in: InterNoise Conference, Hong Kong, 2017.
[19] S. Succi, The Lattice Boltzmann Equation for Fluid Dynamics and beyond, Oxford University Press, New York, NY, USA, 2001.
[20] H. Chen, P. Gopalakrishnan, R. Zhang, Recovery of galilean invariance in thermal lattice Boltzmann models for arbitrary Prandtl number, Internat. J. Modern Phys. C 25 (10) (2014) http://dx.doi.org/10.1142/S0129183114500466.
[21] H. Chen, S. Chen, W.H. Matthaeus, Recovery of the Navier-Stokes equations using a lattice-gas Boltzmann method, Phys. Rev. A 45 (8) (1992).

[22] X. Shan, X. Yuan, H. Chen, Kinetic theory representation of hydrodynamics: A way beyond the Navier-Stokes equation, J. Fluid Mech. 550 (2006) 413–441, http://dx.doi.org/10.1017/S0022112005008153.

[23] V. Yakhot, S.A. Orszag, Renormalization group analysis of turbulence. I. Basic theory, J. Sci. Comput. 1 (1) (1986) 3–51, http://dx.doi.org/10.1007/BF01061452.

[24] V. Yakhot, S.A. Orszag, S. Thangam, T.B. Gatski, C.G. Speziale, Development of turbulence models for shear flows by a double expansion technique, Phys. Fluids A (1992) http://dx.doi.org/10.1063/1.858424.

[25] H. Chen, S.A. Orszag, I. Staroselsky, S. Succi, Expanded analogy between Boltzmann kinetic theory of fluids and turbulence, J. Fluid Mech. 519 (2004) 301–314, http://dx.doi.org/10.1017/S0022112004001211.

[26] H. Chen, Volumetric formulation of the lattice Boltzmann method for fluid dynamics: Basic concept, Phys. Rev. E 58 (3) (1998).

[27] B.E. Launder, D.B. Spalding, The numerical computation of turbulent flows, Comput. Methods Appl. Mech. Eng. 3 3 (2) (1974) 269–289.

[28] M.M. Pervaiz, C.M. Teixeira, Two equation turbulence modeling with the lattice Boltzmann method, in: Proceedings of the 2nd International Symposium on Computational Technologies for Fluid/Thermal/Chemical Systems with Industrial Applications, ASME PVP Division Conference, Boston, MA, USA, 1999.

[29] G. Brès, F. Pérot, D. Freed, Properties of the lattice Boltzmann method for acoustics, in: 15th AIAA/CEAS Aeroacoustics Conference, Miami, FL, USA, 2009, http://dx.doi.org/10.2514/6.2009-3395.

[30] S. Marié, D. Ricot, P. Sagaut, Comparison between lattice Boltzmann method and Navier-Stokes high order schemes for computational aeroacoustics, J. Comput. Phys. 228 (4) (2009) 1056–1070, http://dx.doi.org/10.1016/j.jcp.2008.10.021.

[31] J.E. Ffowcs-Williams, D.L. Hawkings, Sound generation by turbulence and surfaces in arbitrary motion, Phil. Trans. R. Soc. A 264 (1151) (1969) 321–342, http://dx.doi.org/10.1098/rsta.1969.0031.

[32] G. Brès, F. Pérot, D. Freed, A Ffowcs Williams - Hawkings solver for Lattice-Boltzmann based computational aeroacoustics, in: 16th AIAA/CEAS Aeroacoustics Conference, Stockholm, Sweden, 2010, http://dx.doi.org/10.2514/6.2010-3711.

[33] F. Farassat, G.P. Succi, A review of propeller discrete frequency noise prediction technology with emphasis on two current methods for time domain calculations, J. Sound Vib. 71 (3) (1980) 399–419, http://dx.doi.org/10.1016/0022-460X(80)90422-8.

[34] D. Casalino, An advanced time approach for acoustic analogy predictions, J. Sound Vib. 261 (4) (2003) 583–612, http://dx.doi.org/10.1016/S0022-460X(02)00986-0.

[35] D.P. Lockard, An efficient, two-dimensional implementation of the Ffowcs Williams and Hawkings equation, J. Sound Vib. 229 (4) (2000) 897–911, http://dx.doi.org/10.1006/jsvi.1999.2522.

[36] W.C.P. van der Velden, D. Casalino, P. Gopalakrishnan, A. Jammalamadaka, Y. Li, R. Zhang, H. Chen, Jet noise prediction : Validation and physical insight, in: 24th AIAA/CEAS Aeroacoustics Conference, Atlanta, GA, USA, 2018, pp. 1–16.

[37] D. Casalino, A. Hazir, A. Mann, Turbofan broadband noise prediction using the lattice Boltzmann method, AIAA J. 56 (2) (2017) 609–628, http://dx.doi.org/10.2514/1.J055674.

[38] D. Casalino, F. Avallone, I. Gonzalez-Martino, D. Ragni, Aeroacoustic study of a wavy stator leading edge in a realistic fan/OGV stage, J. Sound Vib. 442 (2019) 138–154, http://dx.doi.org/10.1016/j.jsv.2018.10.057.

[39] I. Gonzalez-Martino, D. Casalino, Fan tonal and broadband noise simulations at transonic operating conditions using Lattice-Boltzmann methods, in: 2018 AIAA/CEAS Aeroacoustics Conference, Atlanta, GA, USA, 2018, http://dx.doi.org/10.2514/6.2018-3919.

[40] A. Rubio Carpio, R. Merino Martínez, F. Avallone, D. Ragni, M. Snellen, S. Van Der Zwaag, Experimental characterization of the turbulent boundary layer over a porous trailing edge for noise abatement, J. Sound Vib. 443 (2019) 537–558, http://dx.doi.org/10.1016/j.jsv.2018.12.010.

[41] C. Teruna, F. Manegar, F. Avallone, D. Ragni, D. Casalino, T. Carolus, Noise reduction mechanisms of an open-cell metal-foam trailing edge, J. Fluid Mech. 898 (2020) http://dx.doi.org/10.1017/jfm.2020.363.

[42] S.P. Neuman, Theoretical derivation of Darcy's law, Acta Mech. 25 (1977) 153–170.

[43] D.B. Ingham, I. Pop, Transport Phenomena in Porous Media, first ed., Pergamon, Kidlington, Oxford, UK, 1998, http://dx.doi.org/10.1016/B978-0-08-042843-7.X5000-4.

[44] C. Sun, F. Pérot, R. Zhang, P.T. Lew, A. Mann, V. Gupta, D.M. Freed, I. Staroselsky, H. Chen, Lattice Boltzmann formulation for flows with acoustic porous media, Comptes Rendus Mecanique 343 (10–11) (2015) 533–544, http://dx.doi.org/10.1016/j.crme.2015.07.013.

[45] G. Brès, J.W. Nichols, S. Lele, F.E. Ham, Towards best practices for jet noise predictions with unstructured large eddy simulations, in: 42nd AIAA Fluid Dynamics Conference and Exhibit, New Orleans, LA, USA, 2012.

[46] T. Colonius, S.K. Lele, P. Moin, Sound generation in a mixing layer, J. Fluid Mech. 330 (1997) 375–409, http://dx.doi.org/10.1017/S0022112096003928.

[47] T.J. Mueller, Aeroacoustic Measurements, first ed., Springer-Verlag, Berlin, Germany, 2002, http://dx.doi.org/10.1007/978-3-662-05058-3.

[48] J.R. Underbrink, Circularly symmetric, zero redundancy, planar array having broad frequency range applications, 2001.

[49] P. Sijtsma, R. Merino-Martinez, A.M.N. Malgoezar, M. Snellen, High-resolution CLEAN-SC: Theory and experimental validation, Int. J. Aeroacoust. 16 (4–5) (2017) 274–298, http://dx.doi.org/10.1177/1475472X17713034.

[50] P. Sijtsma, Phased Array Beamforming Applied to Wind Tunnel and Fly-Over Tests, Technical Report NLR–TP–2010–549, National Aerospace Laboratory (NLR), Amsterdam, The Netherlands, 2010, URL www.nlr.nl.

[51] L. Rego, F. Avallone, D. Ragni, D. Casalino, Jet-installation noise and near-field characteristics of jet-surface interaction, J. Fluid Mech. 895 (2020) http://dx.doi.org/10.1017/jfm.2020.294.

[52] C. Brown, J. Bridges, Small Hot Jet Acoustic Rig Validation, Techincal Report NASA/TM-2001-214234, Cleveland, OH, USA, 2006.

[53] R.K. Amiet, Noise due to turbulent flow past a trailing edge, J. Sound Vib. 47 (3) (1976) 387–393, http://dx.doi.org/10.1016/0022-460X(76)90948-2.